 doi:10.20944/preprints202209.0258.v1

Article

Carboniferous-Early Permian Heterogeneous Porous Carbonate Reservoirs Prediction and Sedimentary Analysis in the Central Uplift of the South Yellow Sea Basin

Shuyu Wu [1, 2, 3, 4], Qiliang Sun [5,*], Jun Liu[1, 2, 3, 4], and Jianwen Chen[6]

1 School of Engineering, China University of Geoscience (Wuhan), Wuhan 430074, PR China;
2 Yantai Center of Coastal Zone Geological Survey, China Geological Survey, Yantai 264001, PR China;
3 Chinese Academy of Geological Sciences, Beijing 100037, PR China
4 Laboratory for Marine Mineral Resources, Qingdao National Laboratory for Marine Science and Technology, Qingdao 266061, PR China
5 College of Marine Science and Technology, China University of Geoscience (Wuhan), Wuhan 430074, PR China
6 The Key Laboratory of Gas Hydrate, Ministry of Natural Resources, Qingdao Institute of Marine Geology, Qingdao 266071, PR China
* Correspondence: hnwushuyu@163.com; sunqiliang@cug.edu.cn.

Abstract: Mesozoic-Palaeozoic marine carbonate rocks are important hydrocarbon reservoirs in the Central Uplift area of the South Yellow Sea Basin (SYSB). Due to the lack of boreholes and the great heterogeneity of carbonate reservoirs, the distribution of porous carbonate reservoirs and their related key controlling factors remain unclear. Based on seismic inversion and isotope analysis, this study explores the factors affecting the distribution of porous Carboniferous-Early Permian carbonate reservoirs in the SYSB. In this study, the log-seismic characteristics of porous carbonate reservoirs, sensitive lithology parameters, and physical property parameters are extracted and analyzed. The pre-stack simultaneous inversion technique is applied to predict the lithology properties and physical properties of the porous carbonate reservoirs. Moreover, the sedimentary of carbonate is analyzed using isotopes of carbon, oxygen, and strontium. The results indicate that porous carbonate reservoirs with porosities of 3%~5% mainly occur at the paleo-highland (Huanglong Formation and Chuanshan Formation) and the slope of paleo-highland (Hezhou Formation). The porous carbonate reservoirs of the Qixia Formation are only locally developed. In addition, the study area was dominated by a warm and humid tropical climate from the Carboniferous to Early Permian, with four sea-level eustatic fluctuation indicated by the negative and positive $\delta^{13}C$ excursions. When the sea level fell, the study area was exposed and denuded, and the supply of terrigenous detrital was dominated, which significantly influenced the carbonate deposit and diagenesis. This study highlights that sedimentation was a key factor in controlling the quality of Carboniferous-Early Permian carbonate reservoirs. The methods proposed in this study can be used in other carbonate-dominated strata worldwide.

Keywords: Sedimentary; Heterogeneous porous carbonate reservoirs; Isotope analysis; Carboniferous-Early Permian; Central Uplift of the South Yellow Sea Basin

1. Introduction

Carbonate strata are essential for the hydrocarbon industry, because they contain approximately 70% of the global hydrocarbon reserve, 50% of the proved recoverable reserve, and 60% of the hydrocarbon production [1-4]. Hydrocarbon exploration of marine carbonate has been conducted in China for more than 40 years, and several large marine gas fields, including the Weiyuan [5-7], Puguang [8, 9], Longgang [10, 11], and Yuanba [12, 13] have been discovered in the Sichuan Basin located in the Upper Yangtze Platform

 doi:10.20944/preprints202209.0258.v1

[14-18]. As an extension of the Lower Yangtze Platform in the eastern area, the South Yellow Sea Basin (SYSB) is a multi-cycle superimposed basin on the Pre-Sinian metamorphic basement (Fig 1a). The SYSB has a similar tectono-paleogeography background and stratigraphic characteristics as the petroliferous Upper Yangtze region, whereas it is the last large-scale sedimentary basin offshore China where no commercial hydrocarbon reservoirs have been discovered after long-time explorations [19-22].

The boreholes and reflection seismic data have confirmed that the Mesozoic-Paleozoic marine carbonate rocks were well developed in the Central Uplift of SYSB [23-25]. However, the Mesozoic-Paleozoic strata in the study area have experienced variable exposures and denudations due to intense Indosinian and Yanshan tectonic events [26-28]. In addition, carbonate reservoirs are highly heterogeneous during deposit and diagenesis [29-31], making them highly complex and challenging to be statistically quantified. Therefore, carbonate reservoirs prediction is the key to hydrocarbon exploration in the SYSB, which needs to be further studied [32-34].

In this study, high-quality 3D seismic data and well data are used to explore the controlling factors of Carboniferous-Early Permian carbonate reservoirs properties. This study aims to: 1) characterize the porous carbonate reservoirs through the well log data and seismic reflection data; 2) predict the distribution of favorable carbonate reservoirs; 3) analyze the sedimentary through the isotopes of carbon, oxygen, and strontium; 4) build a model for the distribution of porous carbonate reservoirs. This study will reveal the distribution and controlling factors of porous carbonate reservoirs, and thus contributes to hydrocarbon exploration in the basin.

2. Geology background

The SYSB is located in the East Asian continental margin, the basin is the offshore part of Lower Yangtze Plate, which is located to the north of Qingling-Dabie-Sulu Orogenic Zone and the North China Plate (Fig 1a) and to the south of Jiangshao Orogenic Belt and Yangtze Plate [33, 35, 36]. The SYSB region spans from 121°E to 124°E with an exploration area of ~18×10^4 km^2, the SYSB can be subdivided into five secondary tectonic units, including the Wunansha Uplift, the South Depression, the Central Uplift, the North Depression, and the Qianliyan Uplift from south to north, and they are bounded by regional NE-strike and EW-strike faults [25, 27, 28, 37, 38](Fig 1b). The SYSB stratigraphy comprises Archean- Proterozoic metamorphic rocks, Paleozoic to Triassic marine sediments and Mesozoic- Cenozoic terrigenous sediments [39, 40]. The marine sedimentary sequences are throughout the whole basin, whereas the Mesozoic-Cenozoic continental sedimentary sequences mainly developed within the South Depression and the North Depression [41].

The SYSB underwent six main stages of tectonic evolution: 1) Sinian- Early Ordovician plate expansion (passive continental margin basin) stage; 2) Late Ordovician-Silurian plate convergence, compression and uplift (foreland basin) stage; 3) Late Devonian - Middle Triassic stable platform-intraplate rift stage; 4) Jurassic- Early Cretaceous intracontinental uplift and compression (foreland basin) stage; 5) Late Cretaceous- Oligocene intracontinental extension-faulted stage, and 6) Miocene to Quaternary intracontinental orogenic (depression basin) stage [20, 42]. The tectonic framework of the East Asian continental margin was mainly dominated by the West Pacific, Eurasian, and Indian plate during the Mesozoic- Cenozoic periods [43, 44].

Previous studies suggest that four regional source rocks are developed in the Mesozoic- Paleozoic periods in the SYSB, including the Early Cambrian Hetang Formation, Late Ordovician Wufeng Formation, Early Silurian Gaojiabian Formation, and Late Permian Longtan- Dalong formations [45-47]. Marine-facies reservoir was the main reservoir in the SYSB, including the Late Sinian Dengying Formation, Carboniferous-Late Permian Qixia Formation, and Early Triassic Qinglong Formation [32, 48, 49]. Three complete source-reservoir- caprock assemblages are developed in the SYSB. The first assemblage is composed of the Hetang Formation as the source rock, Late Sinian Dengying Formation and

Ordovician limestones as the reservoirs, and the Late Ordovician Wufeng Formation-Silurian Gaojiabian Formation as the seals [50]. The second assemblage is composed of the Late Ordovician Wufeng Formation- Early Silurian Gaojiabian Formation as the source rocks, Middle-Late Silurian-Late Devonian Wutong Formation and Carboniferous-Early Permian Qixia formation as the reservoirs, Late Permian Longtan-Dalong Formation as the seal [51]. The third assemblage is composed of the Late Permian Longtan-Dalong Formation as the source rock, Early Triassic Qinglong Formation as the reservoir, and the Mesozoic Formation as the seal [52]. Only four wells (CZ35-2-1, CZ12-1-1, WX13-3-1, and CSDP-2) had drilled through the Carboniferous-Early Permian strata [8, 32, 53, 54]. Moreover, some hydrocarbon discoveries were observed in the core samples of the Carboniferous-Early Permian strata from the recent borehole CSDP-2, indicating that the SYSB in this target layer has oil and gas potential [55-57].

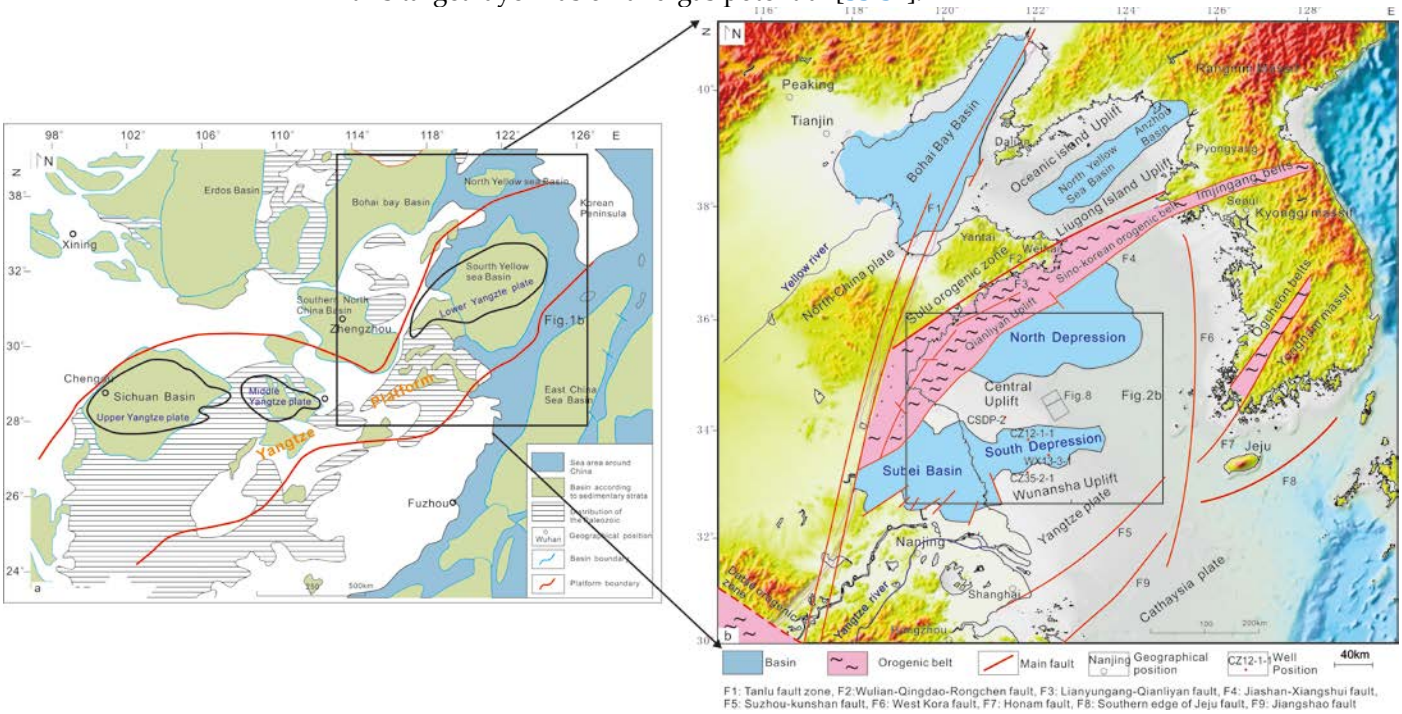

Figure 1. (**a**) Geographical location and tectonic map of the Yangtze block, South China (modified by [22]); (**b**) Geographical location and tectonic map of the SYSB (modified by [58]).

The Carboniferous-Early Permian strata include the Carboniferous Hezhou Formation, Carboniferous Huanglong Formation, Carboniferous Chuanshan Formation, and Permian Qixia Formation (Fig 2a). The SYSB was mainly marine deposition deposited in this period, with limestone and dolomitic limestone lithology (Fig 2b).

Preprints (www.preprints.org) | NOT PEER-REVIEWED | Posted: 19 September 2022 doi:10.20944/preprints202209.0258.v1

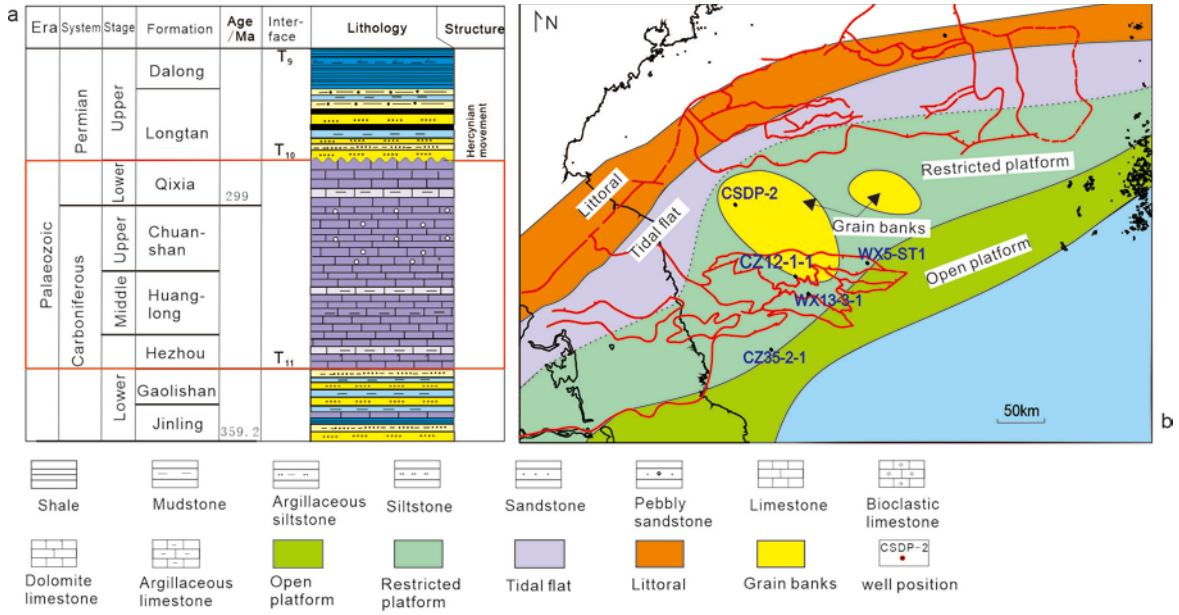

Figure 2. (**a**) Composite bar chart. (**b**) Sedimentary facies of Carbonate Formation.

3. Materials

High-quality 3D seismic data covering an area of 685 km² and consisting of 857 in-lines and 2814 crosslines is used in this study. The bin spacings are 25 m and 37.5 m in the inline and crossline directions, respectively. The seismic data was acquired using a 6390 cubic inch air gun located at a water depth of 10 m and fired at every 37.5 m. Frequency ranges from 0 Hz to 80 Hz, the dominant frequency is ~35 Hz, P-velocity ranges from 5000 m/s to 6000 m/s. The high-resolution and high-fidelity seismic processing workflow (i.e., statics correction, multiple removal, pre-stack noise suppression, deconvolution) has been adopted to obtain the pre-stack time migration data used in this study.

Two wells (CSDP-2 and CZ12-1-1) were used in this study. Borehole CSDP-2 sampled the continuous coring of 2843.18 m and drilled through the Neogene, Triassic, Permian, Carboniferous, and Devonian strata. Borehole CZ12-1-1 has a total depth of 3511 m, drilling through the Neogene and Carboniferous strata (Figs 1b, 2b). The well logs of P-wave velocity, S-wave velocity, and density are used in this study. The sedimentary structure, texture, color and oil bearing property were described on the CSDP-2 borehole, thirty-six (36) core samples of carbon and oxygen isotopes and 18 core samples for the strontium isotope from the CSDP-2 borehole are tested for the sedimentary analysis. samples from bioclastic, secondary fissures, calcite veins, recrystallization, and secondary transformation are excluded in this study, and only pure limestones are tested.

4. Methods

4.1. Porous carbonate prediction

4.1.1. Log-seismic characteristic analysis

The well CZ12-1-1 is used to make the log-seismic characteristic analysis (Fig 3). It was drilled in the Chuanshan Formation from 2069 m to 2212 m, with a thickness of 137 m. The Chuanshan Formation is mainly composed of bioclastic limestone. The P-wave velocity ranges from 5000 m/s to 6000 m/s in this formation, and its density ranges from 2.3 g/cm³ to 2.6 g/cm³. The P-wave impedance is between 16000 g/cm³·m/s and 17000 g/cm³·m/s. The strata (the Sanduo Formation) above the Chuanshan Formation comprises clastic rocks with a P-velocity of 3000 m/s - 4000 m/s and a density of 2.2 g/cm³ - 2.4 g/cm³. Its P-wave impedance ranges from 7000 g/cm³·m/s to 8000 g/cm³·m/s. The P-wave velocity, P-wave impedance, and density of the clastic Sanduo Formation are much lower than

Preprints (www.preprints.org) | NOT PEER-REVIEWED | Posted: 19 September 2022 doi:10.20944/preprints202209.0258.v1

those of the bioclastic limestone of the Chuanshan Formation. The limestone is characterized by low-medium frequency, weak amplitude, and semi-continuous-continuous seismic reflections.

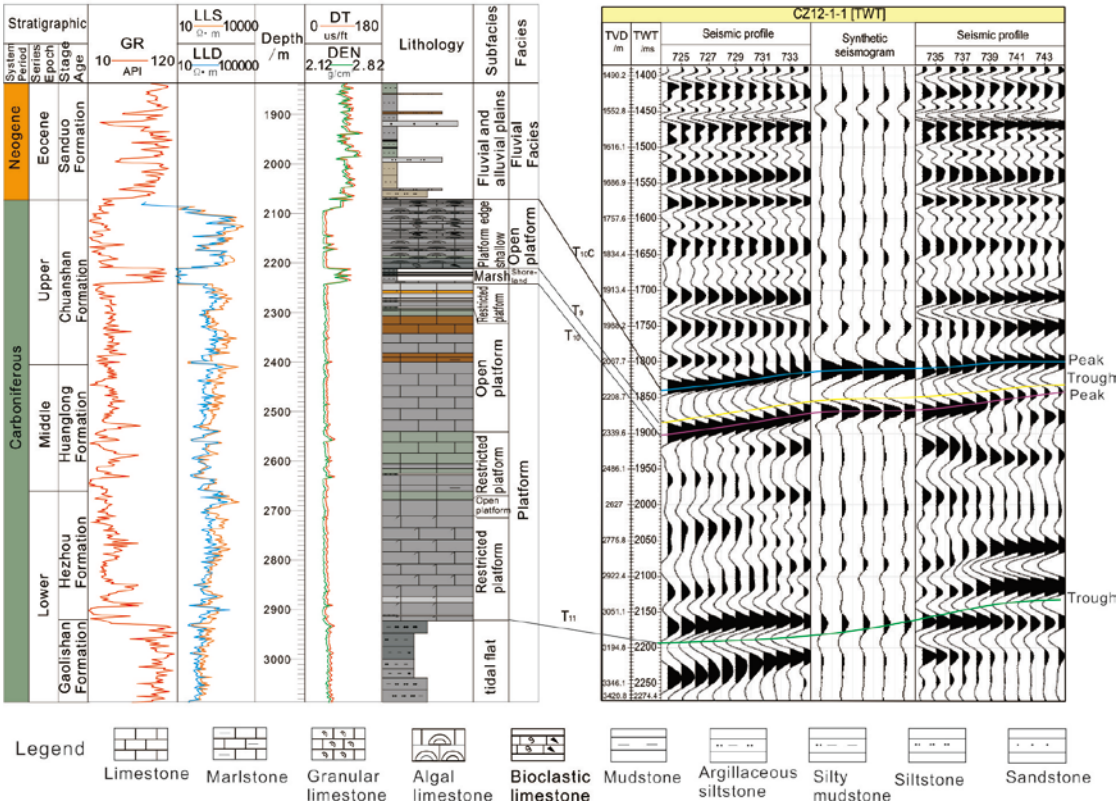

Figure 3. Log characteristic and seismic reflection of bioclastic limestone in well CZ12-1-1

4.1.2. Sensitive parameter extraction

Extract the sensitive parameter of the porous carbonate rock, a total of 15 core samples were taken from the Early Permian to Carboniferous strata (depths from 1647 m to 1960 m) for petrophysical parameter testing. The lithologies of all samples are mainly bioclastic limestone, pure limestone, sandstone, and mudstone, which were analyzed by the MTS815 spectrometer. The facility is equipped with high-precision pressure, displacement, volume change, temperature sensor, and ultrasonic transducers. P-wave velocity and S-wave velocity are tested under strata pressure state, and the test conditions and data collection are controlled by a program of transmission method for measurement, which provides advanced experimental conditions for the test.

From the petrophysical parameter tests, the P-wave velocity, S-wave velocity, and saturated water density were obtained (Table 1; Fig 4). P-wave velocity value ranges between 5075 m/s and 6568 m/s, S-wave velocity value ranges between 2551 m/s and 3432 m/s, and saturated water density value ranges between 2.582 g/cm^3 and 2.761 g/cm^3, respectively. The comparison of the P-velocity of well logging (green dotted line) with that from the petrophysical parameter test (black red bar) shows a good fit between them (Fig 4a), which indicates the accuracy of the test result.

Table 1. P-wave velocity, S-wave velocity, and density of borehole CSDP-2 from petrophysical parameter tested.

Stratum	Depth (m)	Lithology	Formation pressure (MPa)	P-wave velocity (m/s)	S-wave velocity (m/s)	Saturated water density (g/cm^3)

Preprints (www.preprints.org) | NOT PEER-REVIEWED | Posted: 19 September 2022 doi:10.20944/preprints202209.0258.v1

Qixia Fm	1647.5	Argillaceous limestone	37	6568.8	3372.1	2.761
	1667.5	Micrite limestone	37	5864	3257.8	2.677
	1684.1	Mudstone	38	5075.1	2551.7	2.624
	1713.4	Mudstone	38	6270.5	3217.8	2.756
Chuanshan Fm	1733.3	Bioclastic limestone	39	6171	3028.5	2.597
	1767.4	Bioclastic limestone	39	6303.1	3368.5	2.656
	1801.68	Crystallite limestone	40	5931	2947.9	2.596
	1816.5	Crystallite limestone	41	6261.3	3000.6	2.671
Huanglong Fm	1830.18	Micrite limestone	41	6511.4	3160.3	2.617
	1844.9	Micrite limestone	41	5939.2	3431.1	2.603
	1867.1	Micrite limestone	42	6100	3223.4	2.711
	1908.3	Limestone	43	6201.3	3411.8	2.644
Hezhou Fm	1935.8	Limestone	43	5701.7	3341.7	2.618
	1939.85	Clot limestone	43	5628.1	2802.5	2.644
	1958.08	Greyish fine sandstone	44	5183.6	2877.9	2.582

* Fm: formation

Based on the core test data of the well CSDP-2 (Table 1) and the intersection of P-wave impedance and S-wave impedance (Fig 4b), we observe that the P-wave impedance can distinguish the lithology of bioclastic limestone, pure limestone, and clastic rock. P-wave impedance of clastic rock value ranges between 10000 g/cm³·m/s and 14500 g/cm³·m/s. While pure limestone value ranges between 13800 g/cm³·m/s and 16300 g/cm³·m/s, which is general higher than that of clastic rock. The bioclastic limestone has the maximum values that vary from 16300 g/cm³·m/s to 17500 g/cm³·m/s. Therefore, P-wave impedance is a sensitive lithology parameter.

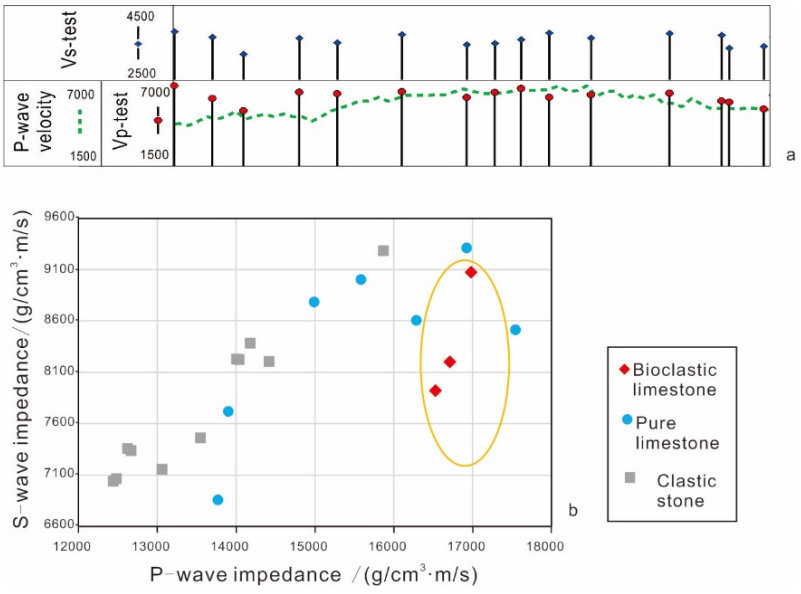

Fig 4. (**a**) P-wave velocites from CSDP-2 well logs and petrophysical parameter test, and S-wave velocity from petrophysical parameter tests; (**b**) Analysis of lithology sensitive parameters in the well CSDP-2.

In order to obtain the physical property-sensitive elastic parameters of the reservoir, the limestone porosity measured from the well CSDP-2 was divided into different equal

Preprints (www.preprints.org) | NOT PEER-REVIEWED | Posted: 19 September 2022 doi:10.20944/preprints202209.0258.v1

sections. According to the petrophysical equations, elastic parameters were calculated from P-wave velocity, S-wave velocity, and density. Afterward, the sensitive elastic parameters of physical properties were screened, providing a reference for further reservoir prediction. The intersection analysis showed that as the porosity increases, the Lamet constant (λ), Poisson ratio (ν) (Fig 5a), P-wave impedance, bulk modulus (K) (Fig 5b), shear modulus (μ), and P-wave velocity (Fig 5c) decrease. However, the differentiation of properties by these elastic parameters alone can result in a certain degree of overlap. The limestone with low Lamme constant *density ($\lambda\rho$) and shear modulus *density ($\mu\rho$) have good physical properties (Fig 5d). The $\lambda\rho$ can clearly distinguish good and poor reservoirs, which was selected to determine the physical properties of the reservoirs. It was intersected with the porosity of limestone in the targeted formation (Fig 5e), obtaining the linear relationship $\varphi = \lambda\rho \times 10^{-9} + 1.3052$.

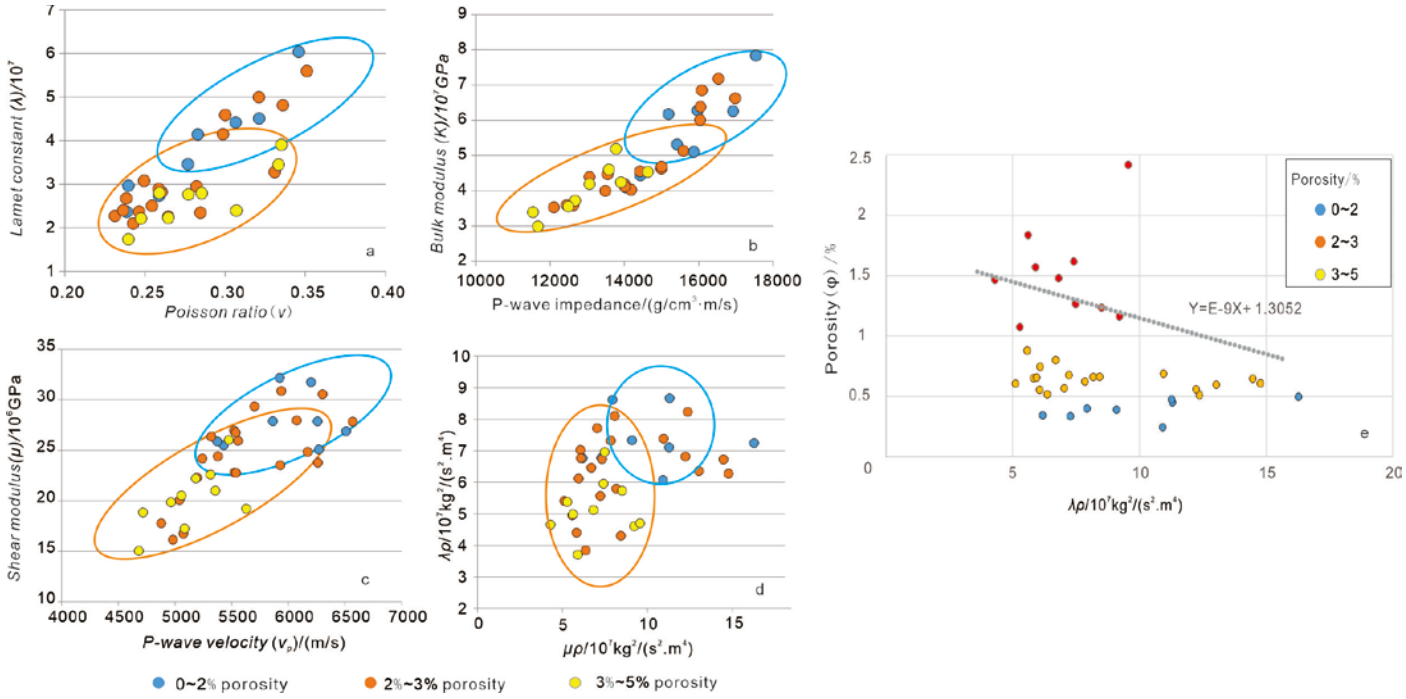

Fig 5. Property sensitive parameters from well CSDP-2. (**a**) Intersection of lamet constant versus passion ratio; (**b**) Intersection of P-wave impedance versus bulk modulus; (**c**) intersection of P-wave velocity versus shear modulus; (**d**) Intersection of shear modulus×density ($\mu\rho$) versus lamet×density ($\lambda\rho$); (**e**) Intersection of lamet×density ($\lambda\rho$) versus porosity of bioclastic limestone of the Carboniferous-Early Permian strata from the well CSDP-2.

4.1.3. Wavelets extraction

The seismic inversion is based on the convolution model. The synthetic trace can be generated from the convolution of seismic reflectivity series with the desired wavelet:

$$S(t) = W(t) * R + N \quad (1)$$

Where $W(t)$ is the extracted statistical wavelet; R is the reflection coefficient (RC) series; N is the random noise. Based on the log curves of the well CSDP-2 and seismic profile (Fig 6), the well-seismic data is calibrated with the following procedure: (a) calibrating the seismic-well using Ricker wavelet, (b) extracting the minimum phase wavelet and the zero-phase wavelet, according to the synthetic records. Seismic frequencies range from 8 Hz to 50 Hz, with a dominant frequency of 25 Hz. Through a large number of synthetic records, the non-zero phase wavelet extracted from a nearby seismic well is found to be the best one. As shown in Fig 6a, the synthetic record of the well CSDP-2

Preprints (www.preprints.org) | NOT PEER-REVIEWED | Posted: 19 September 2022 doi:10.20944/preprints202209.0258.v1

matches the seismic trace, indicating that the extracted wavelet is useful, and thus determining the time-depth relationship of the well. On this basis, the near-middle-far angle gathers are partially superimposed. After well-seismic calibration with three superimposed angle gathers (Fig 6b), the near-middle-far angle wavelets are extracted (Fig 6c).

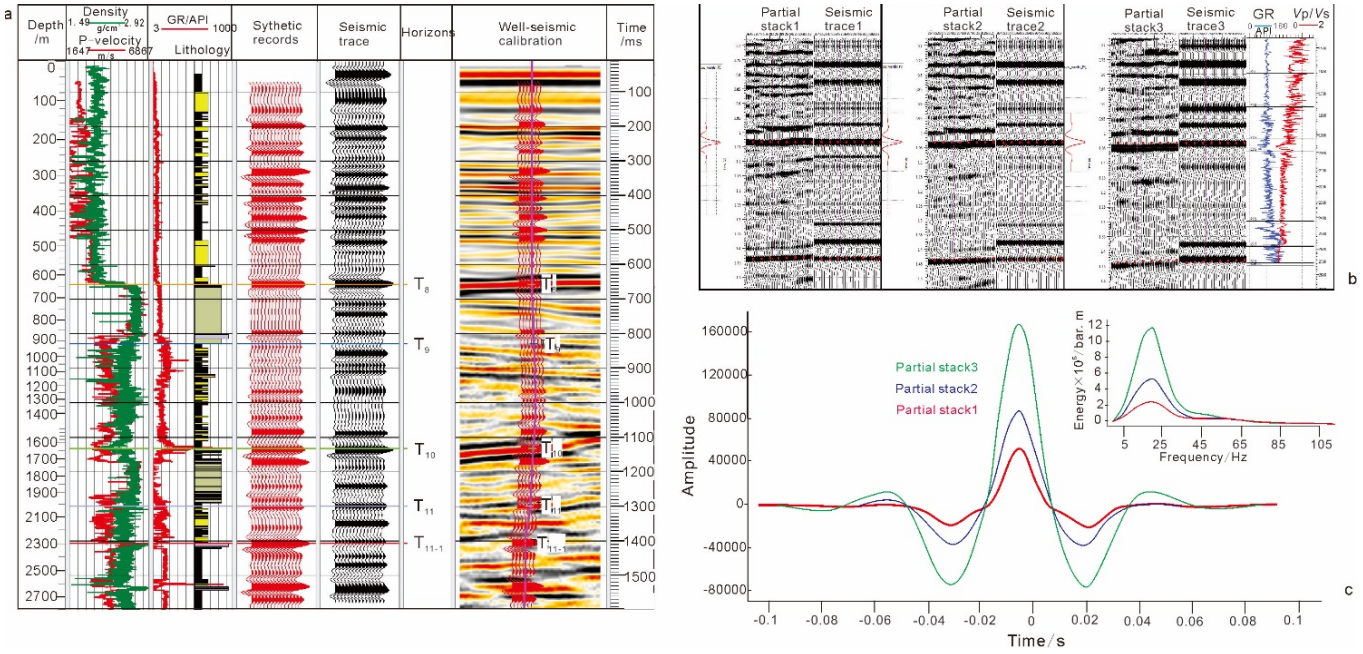

Fig 6. The synthetic seismogram and extracted wavelets of the well CSDP-2. (**a**) Synthetic records from full angle superimposed gathers; (**b**) Synthetic records from the near-middle-far angle superimposed gathers; (**c**) Wavelets extracted from the near-middle-far angle superimposed gathers after well-seismic calibration.

4.1.4. Low-frequency model establishment

Two terms are used to define acoustic impedance: relative acoustic impedance and absolute acoustic impedance [59, 60]. Relative acoustic impedance does not involve the generation of a low-frequency model for its calculation. It is the property of the relative layer for qualitative interpretation. In contrast, absolute acoustic impedance is an absolute layer property used for qualitative and quantitative interpretations [61]. However, marine seismic data in the study area generally lacks frequency information below 8 Hz. Therefore, absolute acoustic impedance can be obtained when a proper low-frequency component (approximately 0-10 Hz) is incorporated in inversion algorithms. In a pre-stack simultaneous inversion, low frequencies are added as part of the inversion algorithm, including low models of P-wave impedance, S-wave impedance, and density. The processes are as follows:

1. The strata framework is established, and the P-wave velocity log curves are spatially interpolated to obtain the initial P-wave velocity low-frequency model;
2. P-wave velocity tomographic inversion is applied, and a P-wave velocity low-frequency model is added;
3. According to the correlation between P-wave velocity, S-wave velocity, and density in the well, the P-wave velocity low-frequency model is converted to the S-wave velocity and the density low-frequency model.

4.1.5. Inversion steps

Due to the diagenesis and tectonism, the Carboniferous-Early Permian SYSB sedimentary facies are diverse in lateral distribution with different physical properties of carbonate rocks. According to the physical characteristics of carbonate rocks in the study

 doi:10.20944/preprints202209.0258.v1

area, an appropriate inversion method was applied to predict the distribution of the favorable reservoirs. In general, the factors affecting inversion results are mainly geological conditions and methods. However, the key factors of methods mainly include the quality of seismic data, wavelet extraction, low-frequency model establishment, and the inversion parameters. Based on petrophysical analysis (lithological and property sensitive elastic parameters), the pre-stack simultaneous inversion method is used to predict Carboniferous-Early Permian carbonate reservoirs. The steps to perform pre-stack simultaneous inversion are as follows:

1. The well-seismic data is calibrated according to near-middle-far angle superimposed gathers to obtain the near-middle-far seismic wavelets;
2. A low-frequency model is established to combine the velocity model of wellpoint spatial interpolation with the high precision tomographic velocity inversion results;
3. Based on the optimized near-middle-far gathers, the pre-stack simultaneous inversion method is applied to predict the lithology properties and physical properties of Carboniferous-Early Permian carbonate reservoirs;
4. The favorable distribution characteristic of porous carbonate reservoirs is obtained in the study area.

4.2. Carbon, oxygen, and strontium isotope analysis

4.2.1. Isotope measurement

Carbon and oxygen isotopes were tested at the State Key Laboratory of Oil and Gas Reservoir Geology and Exploration (Chengdu University of Technology). A Thermo Fisher Stable Gas Isotope Mass Spectrometer MAT 253 with the phosphoric acid method was used. Afterward, strontium isotope analysis was conducted using Triton Plus thermoelectric ionization isotope mass spectrometer.

4.2.2. Validation of stable isotope data

The preservation status of bulk carbonate samples was verified by the correlation between their $\delta^{18}O$ and $\delta^{13}C$ values. Since a strong correlation (R >0.5) suggests diagenetic changes, bulk samples with R >0.5 were altered. The bulk carbonate samples from all investigated sections indicate no significant correlation between $\delta^{18}O$ and $\delta^{13}C$ (R = 0.24; Fig8). Furthermore, the $\delta^{18}O$ value significantly decreased after diagenesis by the interaction of atmospheric fresh water and hydrothermal fluid. When $\delta^{18}O$ <-5‰, the carbonate rocks underwent diagenetic alteration, but their carbon and oxygen isotopic compositions still represented the seawater at that period. When $\delta^{18}O$<-10‰, the rocks underwent a strong diagenetic transformation, and the sample values of carbon and oxygen isotopes are no longer available. From the Early Permian to Carboniferous strata, $\delta^{18}O$ values ranges between -10.55‰ and -5.65‰, with a mean value of -7.4‰. Except for the values of two samples $\delta^{18}O$ <-10‰ (at the depth of 1723.73 m and 1948.5 m), all the other values range from -9.75‰ to -5.65‰ (Fig 7). This indicates that though the oxygen isotopes are affected by diagenesis, they can still represent the original sedimentary.

Preprints (www.preprints.org) | NOT PEER-REVIEWED | Posted: 19 September 2022 doi:10.20944/preprints202209.0258.v1

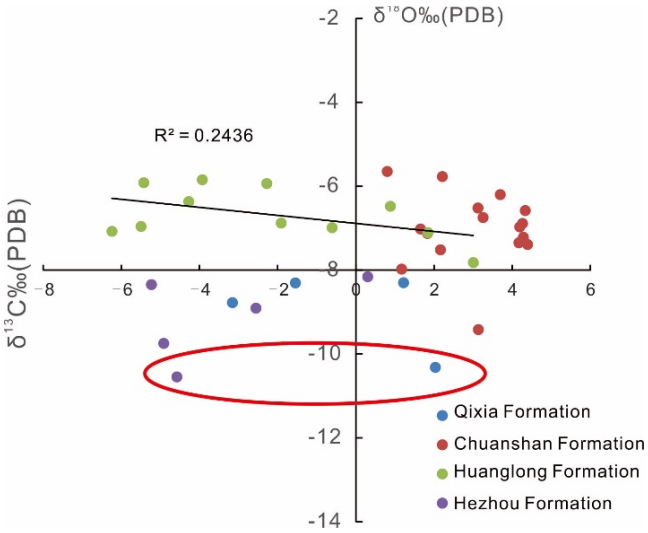

Fig 7. The intersection of $\delta^{18}O$ and $\delta^{13}C$ in the Carboniferous-Early Permian strata.

4.2.3. Paleosalinity

Previous studies have shown that $\delta^{13}C$ and $\delta^{18}O$ generally increased with the paleosalinity [62]. Keith and Weber [63] proposed a calculation formula based on the relationship between the stable isotope and paleosalinity:

$$Z = 2.048(\delta^{13}C + 50) + 0.498(\delta^{18}O + 50)\ (\text{PDB standard}) \quad (2)$$

where Z represents the paleosalinity (Table 2). When Z>120‰, it indicates the seawater-dominated sedimentary; when Z<120‰, it indicates the meteoric water-dominated sedimentary [64-66].

4.2.4. Paleotemperature

Paleotemperature is one of the important factors controlling the stable isotopic composition of carbonate. It can be effectively measured using $\delta^{18}O$ in the following formula [67]:

$$T = 16.9 - 4.2(\delta^{18}O_{CaCO3\text{correct}} + 0.22) + 0.13\ (\delta^{18}O_{CaCO3\text{correct}} + 0.22)^2 \quad (3)$$

In the Paleozoic strata, it is necessary to correct the $\delta^{18}O$ "dating effect". In general, the $\delta^{18}O$ value was calibrated from the average $\delta^{18}O$ of the Quaternary carbonate data (the value is -1.2‰) in Table 2. The average of $\delta^{18}O$ of the Early Permian-Carboniferous strata is -7.7‰, and the difference between them $\Delta\delta^{18}O$ = 6.5‰, $\delta^{18}O_{CaCO3correct}$= measured value - $\Delta\delta^{18}O$. The paleotemperature of seawater can be calculated according to formula (3).

Table 2. Carbon, oxygen isotopic and paleosalinity and paleotemperature

Stratum	Depth(m)	Lithology	$\delta^{13}C_{PDB}$ (‰)	$\delta^{18}O_{PDB}$ (‰)	Paleosalinity (‰)	Paleotemperature (℃)
Qixia Fm	1654.35	Argillaceous limestone	-3.16	-8.78	116.46	16.53
	1658	Argillaceous limestone	1.22	-8.3	125.67	16.30
	1663.03	Argillaceous limestone	-1.55	-8.31	119.99	16.30
	1723.73	Argillaceous limestone	2.03	-10.32	126.32	17.66
	1727.1	Limestone	4.17	-7.35	132.18	16.03

 doi:10.20944/preprints202209.0258.v1

	1728.3	Grey black limestone	4.26	-6.89	132.59	15.98
	1730.4	Grey limestone	4.28	-7.22	132.47	16.01
	1733.3	Dark grey limestone	4.19	-6.97	132.41	15.98
	1746.35	Grey limestone	4.39	-7.39	132.61	16.03
	1747.68	Dark grey limestone	4.33	-6.58	132.89	15.98
	1749.18	Dark grey limestone	3.13	-9.42	129.02	16.92
Chuanshan	1754.8	Dark grey limestone	3.69	-6.2	131.77	16.01
Fm	1757.03	Limestone	3.25	-6.75	130.59	15.98
	1762.28	Grey black limestone	3.12	-6.52	130.44	15.98
	1777.83	Grey black limestone	0.8	-5.65	126.12	16.12
	1786.18	Dark grey limestone	2.21	-5.77	128.95	16.09
	1802.3	Grey black limestone	2.16	-7.52	127.98	16.06
	1810.85	Grey limestone	1.17	-7.98	125.72	16.18
	1814.5	Grey limestone	1.65	-7.02	127.18	15.99
	1815.9	Grey black limestone	1.83	-7.13	127.50	16.00
	1822.7	Brown grey limestone	3	-7.82	129.55	16.13
	1833.65	Grey limestone	-6.24	-7.08	110.99	15.99
	1839.5	Light grey limestone	-0.61	-6.99	122.57	15.99
	1843.45	Grey limestone	0.88	-6.48	125.88	15.98
	1854	Grey limestone	1.84	-7.11	127.53	16.00
Huanglong	1868.53	Grey limestone	-5.5	-6.96	112.57	15.98
Fm	1874.18	Grey limestone	-1.91	-6.88	119.96	15.98
	1881.75	Grey limestone	-4.28	-6.37	115.36	15.99
	1884.58	Grey limestone	-2.28	-5.94	119.67	16.06
	1901.85	Grey black limestone	-5.43	-5.92	113.23	16.06
	1916.45	Grey limestone	-3.93	-5.85	116.34	16.07
	1935.7	Light grey limestone	-5.23	-8.35	112.43	16.32
	1942.95	Light grey limestone	-4.92	-9.75	112.37	17.17
Hezhou Fm	1948.5	Light grey limestone	-4.58	-10.55	112.67	17.88
	1968.53	Limestone	0.3	-8.16	123.85	16.25
	2203.38	Grey limestone	-2.56	-8.91	117.62	16.60

*Fm: formation

5. Results

5.1. Seismic characteristics

The Carboniferous-Early Permian strata is a set of reflection layers between T_{10} and T_{11} in the seismic profiles (Fig 8). Surface T_{10} is the top surface, presenting as moderate-low frequency, high-amplitude positive reflectors. Surface T_{11} is the bottom surface, presenting as moderate-low frequency, high-amplitude negative reflector (Fig 8). The internal seismic reflection of the Carboniferous-Early Permian strata is parallel-subparallel, characterized by moderate-continuous frequency, and moderate-amplitude seismic reflection. The overall formation thickness was relatively stable with a time thickness of 200 ms to 260 ms and a depth thickness of 500 m to 715 m. Due to the influence of the Late

Preprints (www.preprints.org) | NOT PEER-REVIEWED | Posted: 19 September 2022 doi:10.20944/preprints202209.0258.v1

Indosinian tectonic movement, local highlands in the Carboniferous-Early Permian were denuded.

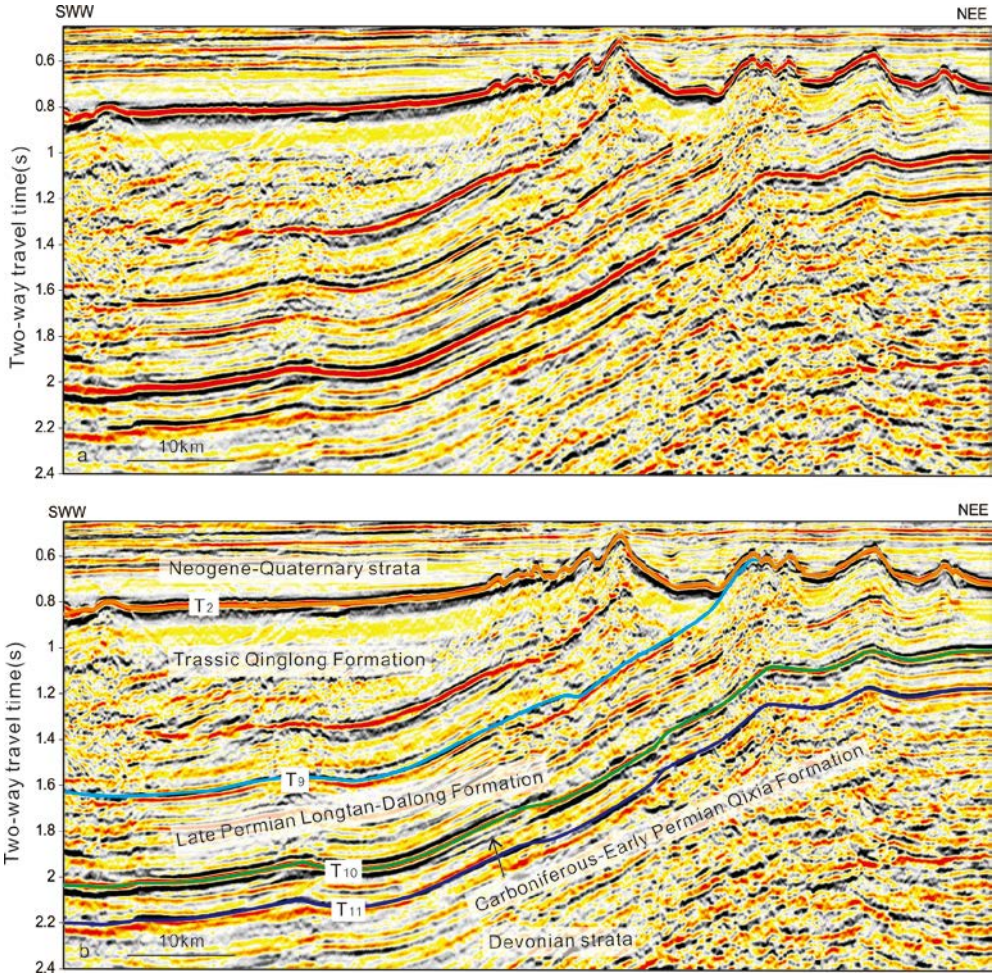

Figure 8. Seismic sequence stratrigratphy and seismic characteristics in the study area.

5.2. Lithological and Petrophysical characteristics

5.2.1. Lithology

Lithology of the lower part of the Hezhou Formation is magenta bioclastic micritic limestone (Fig 9a); the upper part is dominated by fine grey sandstone, and the topmost is medium-coarse lithic quartz sandstone with calcareous. Moreover, the medium-coarse quartz sandstone has high roundness and good sorting. It is supported by a grain structure with the main particle sizes ranging from 0.25 mm to 1 mm. The sedimentary was tidal flat of an open carbonate platform.

Lithology of Huanglong Formation is mainly gray-brown and light grey bioclastic micritic limestone (Fig 9a and Table 3). Bioclastic limestone consists of fusulinida, cephalopods, and brachiopods, with a light flesh-red limestone at the bottom and a small amount of gravel limestone and oolitic limestone. Lithology of lower part is dominantly micritic calcite (Fig 9a). Many silty clastic particles are observed in the micritic calcite crystal aggregates, and the sediments are confined to the platform lagoon environment. Lithology of upper part are characterized by a spherulitic texture with biological fossils. The spherulitic micritic limestone is filled with sparry calcite crystals, and the sedimentary was an open platform shallow beach with high energy turbulence.

Lithology of the Chuanshan Formation is black-grey and dark-grey bioclastic micritic limestone with abundant nucleate stones (Fig 9a and Table 3). The limestone consists of

 doi:10.20944/preprints202209.0258.v1

many bio-fossil fragments filled with micro calcite crystals, the microfracture is well developed between bio-fossil fragments, and the sedimentary was an open platform tidal flat.

Lithology of the lower part of the Qixia Formation is fine-grained clastic rock, with black mudstone intermixed with grey calcareous silt-fine sandstone and thin black coal seams (Fig 9a). The middle part is swinestone, a black bituminous argillaceous limestone, and the upper part is dark-grey limestone (Fig 9a and Table 3). This formation develops fossil spindles and corals, foraminifera, and the sedimentary was a shallow-water carbonate open platform.

Table 3. Strontium isotope of the Carboniferous-Early Permian strata

Stratum	Depth (m)	Lithology	$^{87}Sr/^{86}Sr$
Qixia Fm	1654.35	Argillaceous limestone	0.70870838
	1663.03	Argillaceous limestone	0.70841205
	1723.73	Calcareous mudstone	0.72988313
Chuanshan Fm	1726.5	Ash black limestone	0.70809662
	1730.4	Grey limestone	0.70797393
	1749.18	Dark grey limestone	0.70812883
	1777.83	Ash black bioclastic limestone	0.70877675
	1791	Dark grey bioclastic limestone	0.70836629
	1802.3	Grey bioclastic limestone	0.70858171
	1810.85	Grey bioclastic limestone	0.70867148
	1814.5	Grey bioclastic limestone	0.70855557
	1814.5	Grey bioclastic limestone	0.70863066
	1815.9	Ash black bioclastic limestone	0.70877197
Huanglong Fm	1822.7	Brown grey limestone	0.70860973
	1833.65	Grey limestone	0.7273574
	1854	Grey limestone	0.70858373
	1874.18	Grey limestone	0.70841281
	1901.85	Ash black limestone	0.70854751

* Fm: formation

5.2.2. Types of reservoir space

The Lower Permian-Carboniferous strata are dominated by micritic limestone, and the reservoir space is mainly composed of intergranular porosity, dissolved porosity, stylolite, and fracture.

Intergranular porosity are mainly present in carbonate grains. According to grain types, the porosity can be divided into inter-oolitic porosity, sand porosity, and interclastic porosity. After diagenesis, most of these porosity were filled due to cementation, with bioclast (Figs 9b, k) and spartie calcite (Fig 9l) filling the porosity. Under the single polarized light, the grain shows dark orange light, with only a few residual intergranular porosity observed (Figs 9b, k, l). Some of porosity are filled with calcite or bioclastic limestone (Figs 9d, h), and the others are unfilled (Figs 9c, n, p).

Preprints (www.preprints.org) | NOT PEER-REVIEWED | Posted: 19 September 2022 doi:10.20944/preprints202209.0258.v1

Dissolved porosity are developed in the bioclastic limestone and micrite limestone, which were formed by atmospheric water leaching on the basis of primary porosity. The sizes of porosity vary between 40 μm and 100 μm, and the porosity are connected by dissolution fractures, with most of the dissolution porosity being unfilled (Figs 9e, s).

Stylolite are mainly developed in the micritic limestones with abundant bioclasts. Most stylolite are formed by pressure dissolution and are residual gaps (Figs 9r, u), and some of them are filled with mud. The gaps can be used as hydrocarbon migration channels.

Fractures are developed in the intergranular, stylolite, and fissures. Some fractures are fully filled (Figs 9g, h, j, o) or semi-filled (Fig 9q) with micritic calcite. Moreover, some of them are not filled (Figs 9f, l, m, n, t). The unfilled fractures can be the connection of porosity to increase the permeability of the rock.

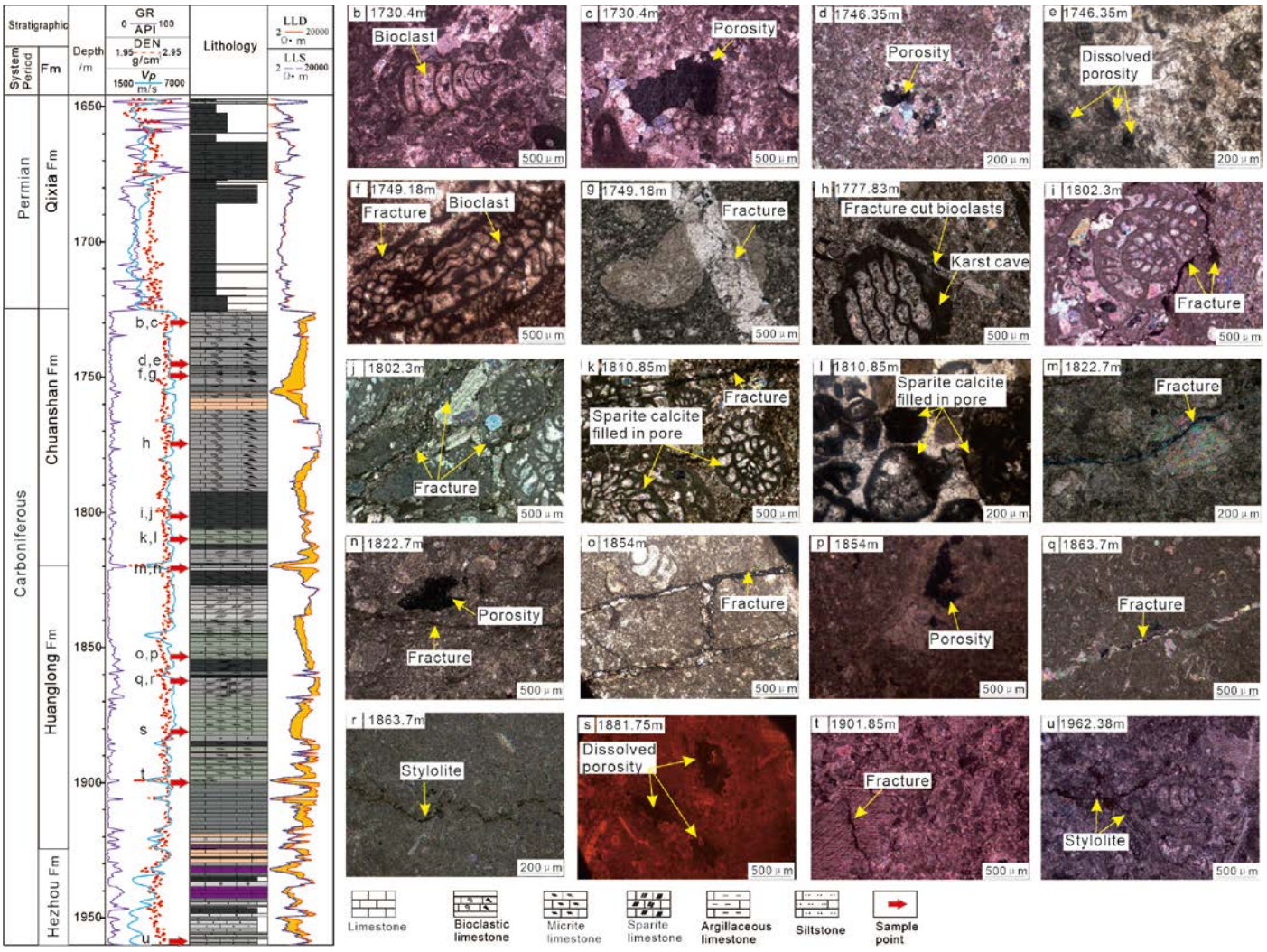

Fig 9. Lithologic column and photos of different types of porosity in the Lower-Permian-Carboniferous strata. (**a**) Lithologic column and logging curve section of the well CSDP-2. Arrows indicate the sample points; (**b**) Bioclastic micritic limestone, shuttle alga fossil at 1730.4 m of Chuanshan Formation (single polarized light); (**c**) Bioclastic micritic limestone, sparry calcite partially filled in the porosity at 1730.4 m of Chuanshan Formation (single polarized light); (**d**) Micrite limestone, sparry calcite partially filled in the porosity at 1746.35 m of Chuanshan Formation (single polarized

 doi:10.20944/preprints202209.0258.v1

light); (**e**) Bioclastic limestone, intergranular dissolution porosity at 1746.35 m of Chuanshan Formation (single polarized light); (**f**) Bioclastic micritic limestone, clay rocks filled in the fracture, clostridium fossils at 1749.18 m of Chuanshan Formation (single polarized light); (**g**) Bioclastic micritic limestone, structural fracture developed, sparry calcite in raw debris at 1749.18 m of Chuanshan Formation (single polarized light); (**h**) Bioclastic micritic limestone, sparry calcite in bioclasts, the large grain size of raw debris, karst cave developed and partially filled with sparry calcite at 1777.83 m of Chuanshan Formation (single polarized light); (**i**) Bioclastic micritic limestone, fracture developed at 1802.3 m of Chuanshan Formation (single polarized light); (**j**) Bioclastic micritic limestone, fractures filled with calcite, visible argillaceous bands at 1802.3 m of Chuanshan Formation (single polarized light); (**k**) Bioclastic micritic limestone, fracture developed, bioclastic coelom porosity filled with sparry calcite at 1810.85 m of Chuanshan Formation (single polarized light); (**l**) Olitic limestone, sparite calcite filled in the porosity with dark orange light at 1810.85 m of Chuanshan Formation (single polarized light); (**m**) Clastic micritic limestone, fracture developed at 1822.7 m of Huanglong Formation (single polarized light); (**n**) Endoclastic micritic limestone, fracture partially filled with argillaceous material, micritic calcite as main interstitial material, dissolution porosity developed at 1822.7 m of Huanglong Formation (single polarized light); (**o**) Micrite limestone, multiple fractures developed, filled with calcite and mud at 1854 m of Huanglong Formation, (single polarized light); (**p**) Micrite limestone, developed crinoids and foraminifera fossil and dissolved pore at 1854 m of Huanglong Formation (orthographic photograph); (**q**) Bioclastic micritic limestone, fracture developed and filled with sparry calcite at 1863.7 m of Huanglong Formation (single polarized light); (**r**) Bioclastic micritic limestone, stylolite developed, partially filled with mud at 1863.7 m of Huanglong Formation (single polarized light); (**s**) Micrite limestone, dissolution porosity developed, cathode luminescence at 1881.75 m of Huanglong Formation; (**t**) Bioclastic sparry limestone, bioclastic rich and fracture developed, fracture partially filled with sparry calcite and mud at 1901.85 m of Huanglong Formation (single polarized light); (**u**) Bioclastic micritic limestone, stoylolite developed, bioclast and stylolite cut by late structural fractures at 1962.38 m of Hezhou Formation (single polarized light).

5.2.3. Reservoir physical property

Based on the core test of 10 samples from the well CSDP-2, the porosities of the Carboniferous strata range between 0.89% and 4.36%, with a mean porosity value of 2.05%, in addition, the permeability ranges between 6.53×10^{-3} mD and 3.80×10^{-3} mD, with a mean permeability of 1.38×10^{-3} mD (Table 4). These petrophysical tests indicate that the reservoir of the Carboniferous strata has low porosity and permeability. Bioclastic micritic limestone in the Chuanshan Formation and Huanglong Formation has high porosities (1.51%-4.36%), while the porosities (0.89%) are low in the Hezhou Formation (Table 4).

Table 4. Petrophysical properties of the Carboniferous Formation.

Stratum	Depth (m)	Lithology	Porosity (%)	Permeability (mD)
Chuanshan Fm	1802.48	Sparite bioclastic limestone	1.51	0.69×10^{-3}
	1807.38	Sparite bioclastic limestone	1.53	0.78×10^{-3}
	1809.65	Bioclastic micritic limestone	2.87	0.65×10^{-3}
	1812.48	Bioclastic microcrystalline limestone	4.36	1.40×10^{-3}
Huanglong Fm	1868.62	Argillaceous microcrystalline limestone	1.49	1.20×10^{-3}
	1892.9	Microcrystalline limestone	1.81	3.8010^{-3}
	1894.08	Bioclastic micritic limestone	1.70	0.15×10^{-3}
	1899.6	Bioclastic micritic limestone	2.99	1.25×10^{-3}
	1904.88	Micritic microcrystalline limestone	1.33	1.16×10^{-3}
Hezhou Fm	1962.38	Bioclastic micritic limestone	0.89	

* Fm: formation

5.3. Porous carbonate distribution

Preprints (www.preprints.org) | NOT PEER-REVIEWED | Posted: 19 September 2022 doi:10.20944/preprints202209.0258.v1

The ultimate goal of seismic inversion is to predict the distribution and physical properties of carbonate reservoirs quantitatively and semi-quantitatively. Base on the pre-stack seismic data at different angle gathers, low-frequency models of P-wave impedance, S-wave impedance, and density are used to constrain and apply the pre-stack simultaneous inversion, and thus obtains the lithology property and physical property of elastic parameters data (Figs 10a, b).

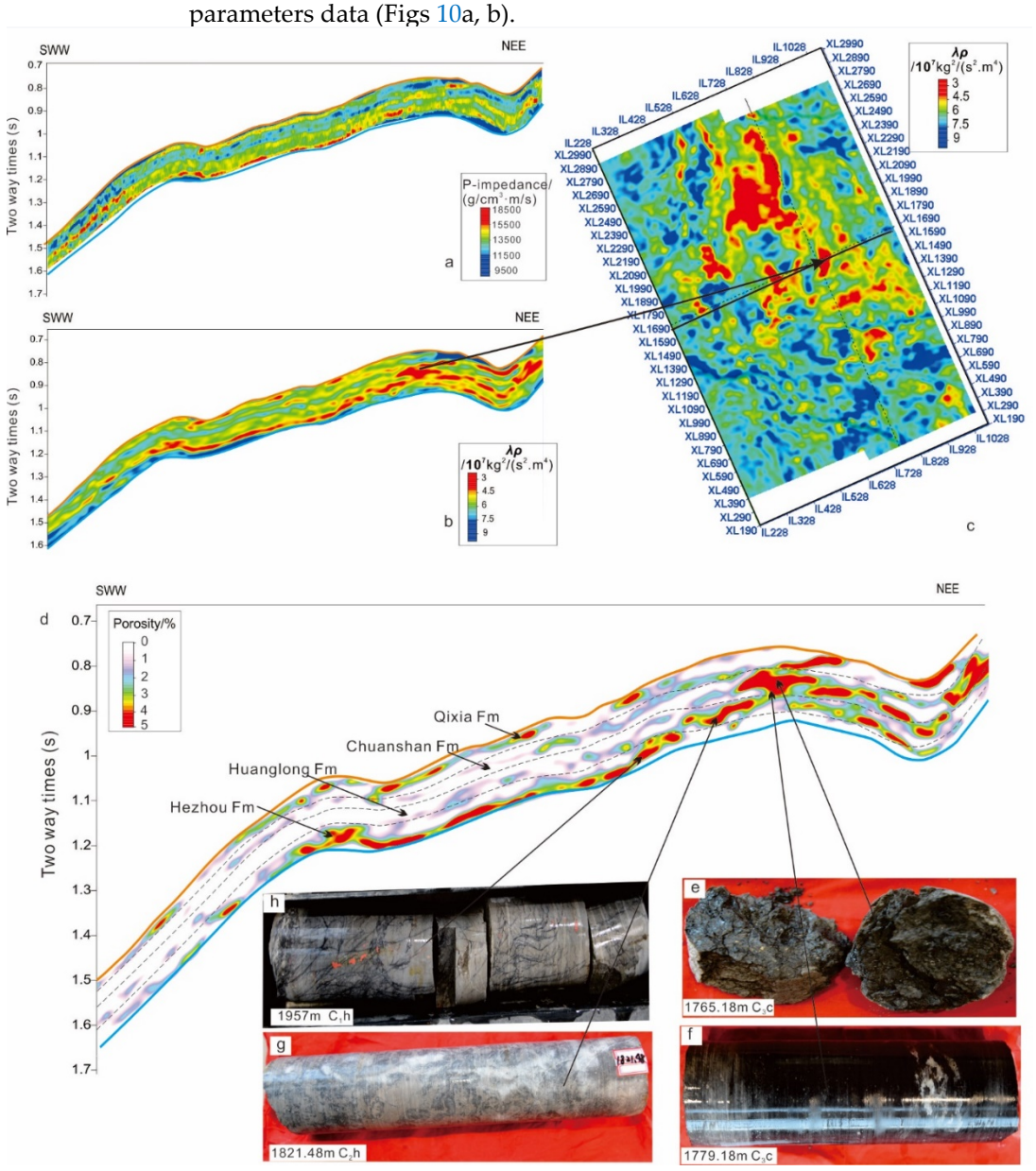

Figure 10. Carboniferous-Early Permian porous carbonate reservoirs prediction. (**a**) P-wave impedance profile showing the lithologic distribution; (**b**) $\lambda\rho$ profile showing the physical properties; (**c**) Physical propertie characteristics of Carboniferous-Lower Chuanshan Formation; (**d**) Porosity profile; (**e**) Oil traces in the Grey-brown bioclastic limestone at the depth of 1765.18m of borehole CSDP-2; (**f**) Oil trace in the dark grey bioclastic limestone at the depth of 1779.18m of borehole CSDP-2; (**g**) Oil immersion in the grey-black bioclastic limestone; (**h**) Oil traces in the grey-black micritic limestone at the depth of 1821.48m of borehole CSDP-2.

According to the results of petrophysical analysis, the threshold of P-wave impedance (13500 g/cm^3·m/s) is used to distinguish clastic rock from limestone, and the threshold of P-wave impedance (16300 g/cm^3·m/s) is used to distinguish bioclastic limestone from

 doi:10.20944/preprints202209.0258.v1

pure limestone. It can be observed that the bioclastic limestone reservoirs of the Carboniferous-Early Permian strata are well developed, mainly in the Hezhou Formation and the Chuanshan Formation, partly in the Qixia Formation (Fig 10a).

From Fig 5d, the physical properties $\lambda\rho$ ranging between 3×10^7 ($kg^2/m^2{\cdot}s$) and 7×10^7 ($kg^2/m^2{\cdot}s$) are the favorable reservoirs in the limestone. Red and yellow colors represent optimal physical properties, and green and blue colors indicate poor physical properties (Fig 10b). According to the P-wave impedance threshold, the impedance range of clastic rock and pure limestone is excluded, and the relationship between $\lambda\rho$ and porosity is obtained based on the results of petrophysical analysis (Fig 5e). Finally, the porosity data of bioclastic limestone reservoirs are obtained (Fig 10c). The result shows that the Carboniferous-Early Permian porous carbonate reservoirs exhibit strong spatial heterogeneity. For vertical distribution, good reservoirs are mainly developed on the slope of the Hezhou Formation, the paleo-highland of the Huanglong Formation and Chuanshan Formation (Fig 10d). In lateral distribution, the carbonate reservoirs with good physical properties is located around the NE-oriented paleo-highland (Fig 10c), with porosity values ranging from 3% to 5%.

According to CSDP-2 borehole, oil traces were observed in the fissures, the middle of grey-brown bioclastic limestone (Fig 10e), and the bottom of dark grey bioclastic limestone (Fig 10f). Oil immersion was also found in the grey-black bioclastic limestone with siliceous bands at the top of the Huanglong Formation. It was also detected in the algal limestone in the middle of the Huanglong Formation (Fig 10g). Furthermore, oil traces were found in the grey-black micritic limestone at the top of the Hezhou Formation, where numerous fractures were developed (Fig 10h). The drilling results are consistent with the reservoir prediction.

5.4. Sedimentary analysis

Carbon isotope ranges between -7‰ and 5‰, with a mean value of 0.158‰; the paleosalinity ranges between 110‰ to 132‰, with a mean value of 124‰. Whilst the paleotemperature vary between 15 ℃ and 18 ℃, with a mean value of 16.0 ℃ (Fig 11; Table 2). Therefore, the sedimentary of SYSB was mainly in a warm and humid subtropical climate [68]. Oxygen isotope are almost representative of the primary sedimentary, with $^{87}Sr/^{86}Sr$ ratios ranging between 0.71 and 0.73 and a mean value of 0.71 (Fig 11; Table 4). Overall, the $^{87}Sr/^{86}Sr$ ratios of test samples are significantly higher than the mantle-derived $^{87}Sr/^{86}Sr$ ratio with an average value of 0.70. The high $^{87}Sr/^{86}Sr$ ratio may indicate the influence of terrigenous diagenetic fluids and clastic types of cement with higher $^{87}Sr/^{86}Sr$ ratio on carbonate [69].

The paleotemperature of the Hezhou Formation increased from 16.2 ℃ to 17.8 ℃ at first and then decreased from 17.8 ℃ to 16.3 ℃. Two negative $\delta^{13}C$ excursion values accompany the decline and rise of the two paleosalinities of the ocean and the last one along with sea level falling [58]. In general, it was a warm and humid climate, mainly in atmospheric water digenetic environment (Fig 12), which is hypoxic in the early stages and oxygen-rich in the late stages [70].

The paleotemperature of the Huanglong Formation is stable and ranged from 15.9 ℃ to 16.1 ℃, the oxygen isotopes ranges from -7.82‰ to -5.94‰, indicating the whole marine deposition remained warm and oxygen-rich (Fig 11). In a atmospheric water digenetic environment, two negative and positive values of $\delta^{13}C$ were exhibited (Fig 12), accompanied by paleosalinity variations in the marine phase (a value ranging from 110.9‰ to 129.5‰), responding to sea-level eustatic [71]. A set of black and grey limestone was deposited during the last transgression after regression (Fig 11), and the Huanglong Formation mainly deposited tight limestone, including micritic limestone and sparite limestone. Remarkably, the last sea-level regression had a high $^{87}Sr/^{86}Sr$ ratio (Table 4).

During the Chuanshan period, the sea level continuously rose [23] with a paleosanity >120‰ (Fig 11), indicating the occurrence of marine sediments. During the Middle-Late Chuanshan period, paleotemperature rapidly decreased. The sea level began to rise in the

next stage, and the whole marine strata were in an oxygen-rich environment. At the end of the Chuanshan period, the sea level reached its maximum, and the $\delta^{18}O$ experienced an abnormally negative shift, accompanied by a high $^{87}Sr/^{86}Sr$ ratio.

At the beginning of the Qixia period, the sea level started to fall [72, 73], accompanied by a decrease in paleosalinity and paleotemperature. Due to limited samples, the sequence stratigraphy is not well controlled. However, the $\delta^{18}O$ value was generally negative (Table 2; Fig 11), and the whole Qixia Formation was in a marine and continental inter sedimentary under an anoxic state [74], where most marine organisms became extinct, and the lithology mainly consisted of black mudstone and limestone (Fig 9a), with the increase of $\delta^{18}O$ value and $\delta^{13}C$ value in the late period, marine organism gradually recovered.

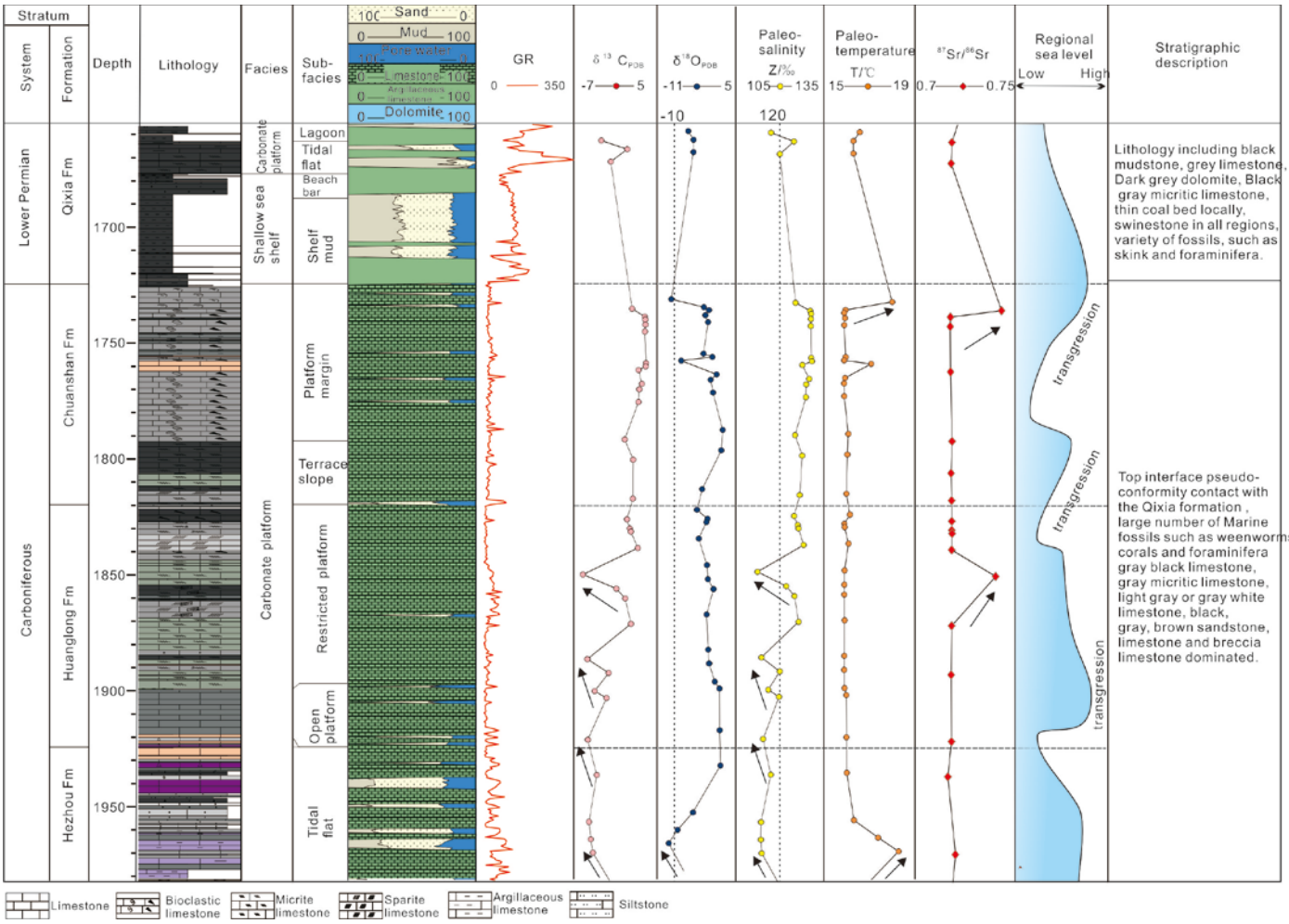

Figure 11. Carbon, oxygen, and strontium isotope compositions of the Carboniferous-Early Permian strata

 doi:10.20944/preprints202209.0258.v1

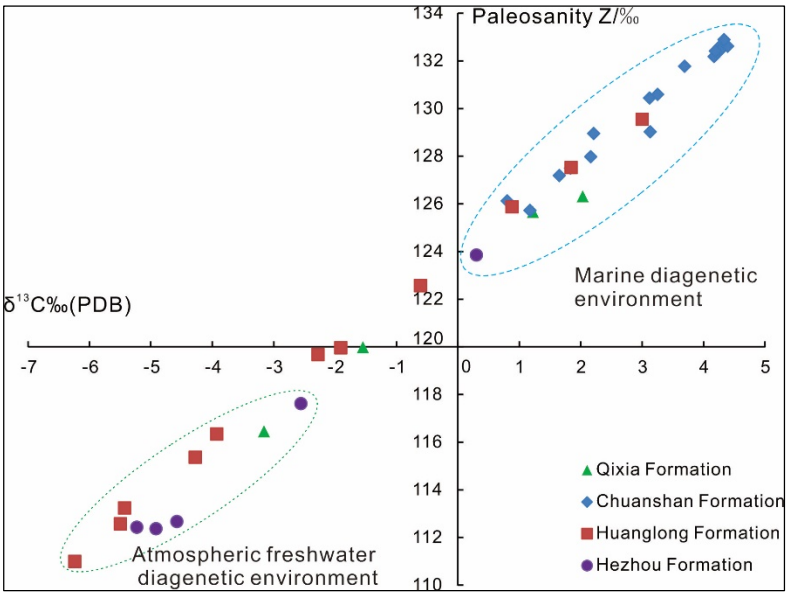

Figure 12. The intersection of carbonate versus paleosalinity of the Carboniferous - Early Permian strata.

6. Discussion

Yangtze Plate is located near the equator in the southern hemisphere, on the eastern edge of the Paleotetheyan ocean during the Carboniferous - Early Permian, with the latitude ranging from 1.6°S to 2.4°N [68, 75-77]. In the Early Carboniferous global transect, the Lower Yangtze Plate and Cathaysia Plate were joined as a large carbonate platform until the end period of the Chuanshan Formation. The tropical climate was warm and humid with abundant atmospheric precipitation, conductive to carbonate deposition [74, 78, 79]. Previous studies of lower latitude Carboniferous-Early Permian sedimentary squences of South China [80-82], North America [83-85] and Euramerica [86] indicated that the sequence architecture and implied eustatic fluctuations of the lower latitude regions (e.g. South China and southwestern USA) correspond well with the Late Palaeozoic Gondwanan glaciation.

The Central Uplift of SYSB was considered a paleo-uplift after the Caledonian period, and the well CSDP-2 revealed a shoal-reef facies developed in local highlands [87, 88](Fig 2b). However, the sea level of the Lower Yangtze Plate in Carboniferous was deeper than that of the Upper Yangtze Plate [87]. Therefore, shoal reef facies of porous reservoirs were mainly developed in the margin of platform uplift in the SYSB, which was enclosed by an open shelf.

The SYSB began to subside in the early period of Carboniferous [89]. During the late of Early Carboniferous, seawater intruded from the east and west sides of the basin. The SYSB was a shallow shelf and tidal-flat environment with an NNE trend during the Hezhou Formation [90]. During the marine sedimentary, delta sedimentary facies were formed nearby the shore (Fig 13a). According to the lithology analysis, terrigenous detrital rocks and carbonate rocks are deposited interbedded in the marine sedimentary. As sea level decreases, sedimentary paleo-uplift were susceptible to superimposed syngenetic and quasi-syngenetic exposures [91](Fig 11h). It was subjected to diagenetic alteration and affected by leaching and dissolution of the freshwater, leading to the increase of pore space [30, 92-97]. Considering there was more accumulation space in the SW slope zone, the shoals began to superimpose and continuously migrate seawards, and shoal reservoirs were well developed and distributed in the slope zone (Fig 10d).

The scale of transgression was the largest in the Huanglong period, and the Yangtze Sea and the Paleo-South China Sea were almost connected, which was a neritic carbonate sedimentary [98] . The open platform, platform margin, restricted platform, and tidal-flat

 doi:10.20944/preprints202209.0258.v1

facies were developed in the SYSB (Fig 13b). Three regression and transgression happened in this period [91], and thus the SYSB periodically exposed, and some of the strata suffered different degrees of denudation. At the end of the Huanglong Formation, the strata suffered from enduring denudation, and its top was a karst weathering crust [98]. As a result, the Huanglong Formation and the overlying strata were in pseudo conformity contact [88, 99]. The high ratio of $^{87}Sr/^{86}Sr$ in the last regression indicated more terrigenous organic matter was carried into the sea water, which resulted in a large negative $\delta^{13}C$ excursions at the sea surface and deep marine. This result may be due to changes in ocean circulation associated with the closure of the western end of the Paleotenthy during the formation of Pangaea [100, 101]. In the high-frequency oscillation environment of the marine deposition, the paleo-highland was characterized by high wave agitation energy. The intergranular porosity were well-developed through leaching and dissolution by the atmospheric precipitation in the late period, leading to a higher porosity in the paleo-highland. In contrast, in the lowlands below the sea level for a long time, the tight lithology was deposited. These areas were not susceptible to dissolution by meteoric water, resulting in a low development of primary pore space (Fig 10d).

During the Late Carboniferous Chuanshan period, seawater intrusion and sediment migration to the SE formed a NE-trending tectonic pattern. From eastern to western part of the basin, open platforms, restricted platforms, and tidal-flat facies are deposited, with organic reef shoal sub-facies developing in local highlands (Fig 13c). In this period, a large amount of bioclastic limestone was deposited due to the low sea level. The primary sedimentary conditions were good, with little diagenesis influence and largely preserved primary sedimentary porosity (Fig 9). The reservoir was partially good in the highlands (Fig 10d). The end of the Chanshan period indicates an anoxic event due to temperature rising at the Carboniferous-Permian transition [102].

The Asselian- Early Sakmarian environment of the South China was a massive epicontinental sea, as a regionally stable carbonate platform [103], The Early Permian was the largest transgression period in SYSB [72, 73], depositing extensive bioclastic limestone rich in fusulinida, corals, foraminifera, and calcareous algae (Figs 9, 10). It formed stable lithofacies and thick carbonate rocks (Hu, 2010). In the late period of the Early Permian, the Lower Yangtze Plate began to retreat, and most of the Lower Yangtze region turned into deltas and lagoons-bay facies, indicating the end of the marine sedimentary history (Fig 13d). With the regression of sea level, the reservoir of Qixia Formation was not well developed (Fig 11d), and the large set of black mudstone mainly served as source rock [104].

As mentioned above, the Central Uplift was an inherited paleo-uplift from the Caledonian movement, with a warm and humid tropical climate and abundant atmospheric precipitation at that time. The favorable conditions for developing porous carbonate rocks are as follows. Firstly, shoal carbonate facies were mainly developed in the paleo-highland. The primary porosity were intergranular, biologic cavity, and biologic skeleton porosity, which formed in a high-energy environment. Secondly, during the syngenetic to quasi-syngenetic period, dissolution occurred after the deposition of the shoal facies. The influence of meteoric water on the diagenetic process was mainly in the early diagenetic and epigenetic periods (terrestrial detrital and the meteoric water in the syngenetic stage). Secondary porosity after the exposure of highlights, mainly composed of dissolved porosity, intergranular porosity, and intragranular porosity, which were more conducive to the preservation of porosity.

Preprints (www.preprints.org) | NOT PEER-REVIEWED | Posted: 19 September 2022 doi:10.20944/preprints202209.0258.v1

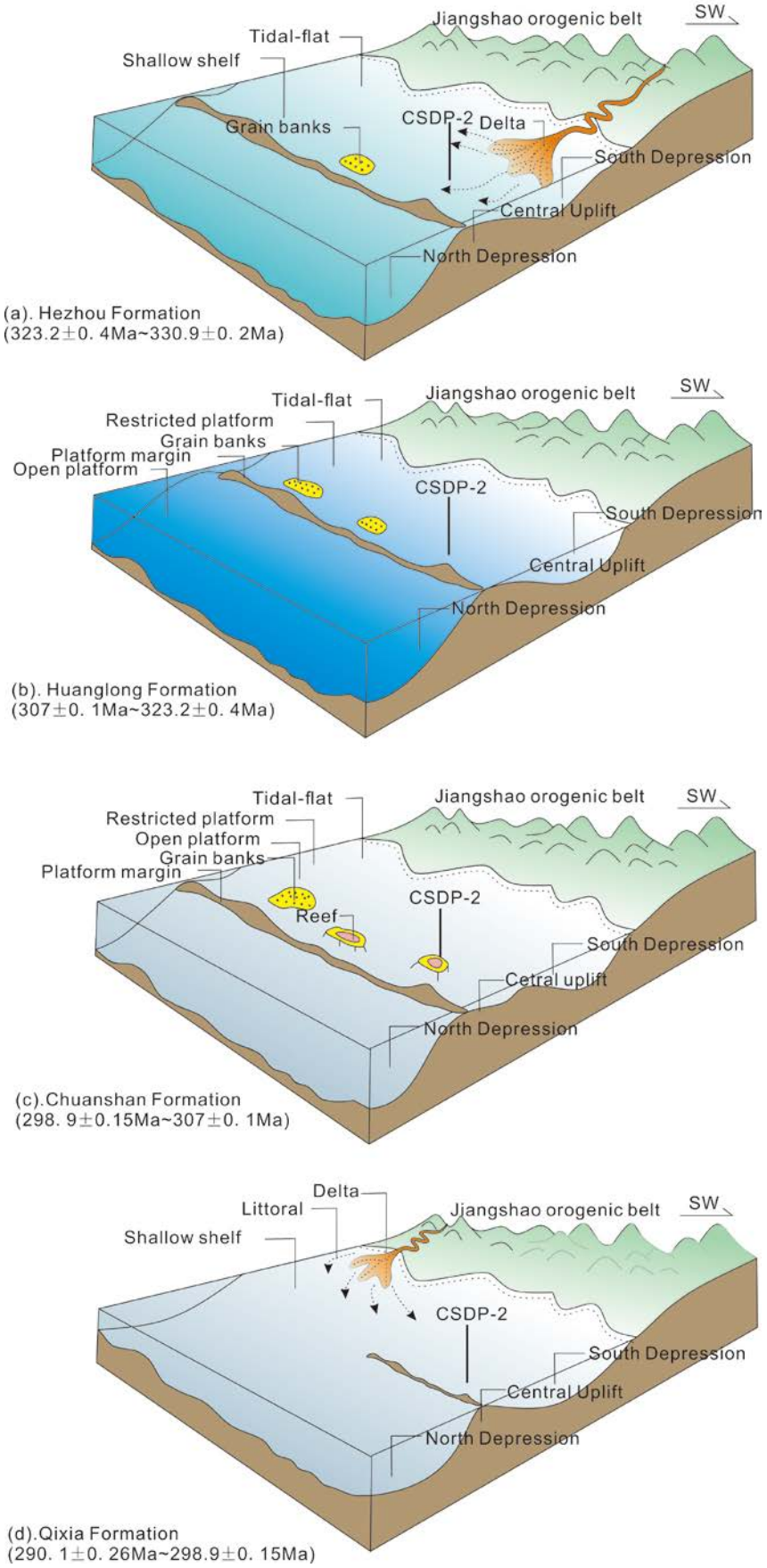

Fig 13. Evolution of Carboniferous - Early Permian sedimentary

7. Conclusions

1. According to the petrophysical analysis, P-wave impedance is a sensitive elastic parameter that can distinguish bioclastic limestone from pure limestone and clastic rock. In addition, $\lambda\rho$ is a physically sensitive elastic parameter, which decreases with increasing porosity;
2. The pre-stack simultaneous inversion method can effectively predict the porous carbonate reservoirs. The results show that the Carboniferous-Early Permian bioclastic limestone was well developed in the Central Uplift of the SYSB, such as on the slope of the Hezhou Formation, paleo-highlands of the Huanglong Formation and the Chuanshan Formation. Moreover, the bioclastic limestone was also locally developed in the Qixia Formation around the paleo-highland with porosities of 3%-5%;
3. According to carbon, oxygen, and strontium isotope analysis, the Carboniferous-Early Permian period was characterized by a warm and humid tropical climate, abundant atmospheric precipitation, and alternating oxygen-rich and hypoxia. From the Hezhou Formation to the Huanglong Formation, there were four negative and positive δ13C excursions, indicating that the carbonate strata was exposed for a long time and suffered from intense denudation. Terrigenous detrital was brought into the seawater in the early Hezhou Formation and at the end of the Huanglong Formation, affecting the carbonate diagenesis.
4. The good physical properties (reservoirs) of porous carbonate in the study area are mainly related: a) the Central Uplift was a successor paleo-uplift after the Caledonian movement, which formed a shoal facies in the paleo-highland; b) due to the fluctuant sea level, the carbonate strata was leached and dissolved by meteoric water during the syngenetic to quasi-syngenetic period. The secondary porosity were enlarged, leading to the development of high-quality reservoirs in local strata. Therefore, leaching and dissolution in the diagenetic period are important factors for good reservoirs.

8. Patents

This section is not mandatory but may be added if there are patents resulting from the work reported in this manuscript.

Supplementary Materials: The following supporting information can be downloaded at: www.mdpi.com/xxx/s1, Figure S1: title; Table S1: title; Video S1: title.

Author Contributions: Shu-yu Wu contributed presented idea, took the lead in writing the manuscript; Qi-liang Sun contributed in supervision and writing of this work; Jian-wen Chen provide the original data; Jun Liu performed the analytic calculations and performed. All authors discussed the results and contributed to the final manuscript. All authors have read and agreed to the published version of the manuscript.

Funding: This study was supported by projects of the China Geological Survey entitled "Geological survey on tectonic and sedimentary conditions of Laoshan uplift" (DD2016015), and the project entitled "Study on Hydrocarbon Accumulation Failure and Fluid Evolution Reduction of the Permian Reservoir in the Laoshan Uplift, South Yellow Sea" (42076220) organized by the National Natural Science Foundation of China.

Data Availability Statement: Qingdao Institute of Marine Geology, China Geological Survey for providing basic data

Acknowledgments: The authors would like to express their gratitude to the Ph. D Jianwen Chen for his help in this study. The authors are also grateful to the editors and reviewers who provided sincere comments and assisted in writing this manuscript.

Conflicts of Interest: The authors declare that they have no known competing financial interests or personal relationships that would have appeared to influence the work reported in this paper.

References:

1. Luo, P.; Zhang, J.D.; Liu, W.; Song, J.M.; Zhou, G.; Sun, P.; Wang, D.C., Characteristic of Marine Carbonate Hydrocarbon Reservoirs in China. *Earth Science Frontiers (China University of Geoscience, Beijing; Peking University)*. **2008**, 15, (1), 36-50.
2. He, Z.L.; Wei, X.C.; Qian, Y.X.; Bao, Z.M.; Fan, M.; Jiao, C.L.; Peng, S.T.; Chen, D., Forming Mechanism and Distribution Prediction of Quality Marine Carbonate Reservoirs. *Oil & Gas Geology*. **2011**, 32, (4), 489-498.
3. Zhao, W.Z.; Hu, S.Y.; Liu, W.; Wang, T.S.; Li, Y.X., Petroleum Geological Features and Exploration Prospect in Deep Marine Carbonate Strata Onshore China: A Further Discussion. *Natural Gas Industry*. **2014**, 34, (4), 1-9.
4. Li, Y.; Kang, Z.J.; Xue, Z.J.; Zheng, S.Q., Theories and Practices of Carbonate Reservoirs Development in China. *Petroleum Exploration and Development Online*. **2018**, 45, (4), 712-722.
5. Wei, G.Q.; Chen, G.S.; Du, S.M.; Zhang, L.; Yang, W., Petroleum Systems of the Oldest Gas Field in China: Neoproterozoic Gas Pools in the Weiyuan Gas Field, Sichuan Basin. *Mar Petrol Geol*. **2008**, 25, (4-5), 371-386.
6. Zhou, Q.; Xiao, X.M.; Tian, H.; Pan, L., Modeling Free Gas Content of the Lower Paleozoic Shales in the Weiyuan Area of the Sichuan Basin, China. *Mar Petrol Geol*. **2014**, 56, 87-96.
7. Wang, Q.T.; Wang, T.L.; Liu, W.P.; Zhang, J.; Feng, Q.; Lu, H.; Peng, P.A., Relationships among Composition, Porosity and Permeability of Longmaxi Shale Reservoir in the Weiyuan Block, Sichuan Basin, China. *Mar Petrol Geol*. **2019**, 102, 33-47.
8. Zhang, X.H.; Guo, X.W.; Wu, Z.Q.; Xiao, G.L.; Zhang, X.H.; Zhu, X.Q., Preliminary Results and Geological Significance of Well CSDP-2 in the Central Uplift of South Yellow Sea Basin. *Chinese Journal Geophysics*. **2019**, 62, (1), 197-218.
9. Lu, P.; Luo, P.; Wei, W.; Zhu, C., Effects of Gas Saturation and Reservoir Heterogeneity on Thermochemical Sulfate Reduction Reaction in a Dolomite Reservoir, Puguang Gas Field, China. *Mar Petrol Geol*. **2022**, 135, 105402.
10. Qin, S.F.; Yang, Y.; Lv, F.; Zhou, H.; Li, Y.X., The Origin of Gas in the Changxing-Feixianguan Gas Pools in the Longgang Gas Field in the Sichuan Basin, China. *Journal of Natural Gas Geoscience*. **2016**, 1, (5), 327-334.
11. Huang, C.S.; Zhang, J.J.; Hu, G.C.; Zhang, L.J.; Chen, H.B.; Wei, D.Y.; Cai, D.; Yu, Y.J.; Li, X.; Ding, P.; Li, J., Characterization of the Distribution, Source, and Potential Ecological Risk of Perfluorinated Alkyl Substances (PFASs) in the Inland River Basin of Longgang District, South China. *Environ Pollut*. **2021**, 287, 117642.
12. Guo, T.L., Hydrocarbon Accumulation Conditions and Key Technologies for Exploration and Development of Yuanba Gas Field. *Petroleum Research*. **2018**, 3, (4), 293-305.
13. Guo, X.H.; Hu, D.F.; Li, Y.P.; Duan, J.B.; Ji, C.H.; Duan, H., Discovery and Theoretical and Technical Innovations of Yuanba gas Field in Sichuan Basin, SW China. *Petroleum Exploration and Development Online*. **2018**, 45, (1), 15-28.
14. Ma, Y.S.; Guo, X.S.; Fang, R., Reservoir Prediction of Feixianguan Formation in Puguang Gas Field, Northeast Sichuan Province. *Petrol Explor Dev+*. **2005**, 32, (4), 60-64.
15. Ma, Y.S.; Cai, X.Y.; Zhao, P.R.; Feng, Z.X., Formation Mechanism of Deep-Buried Carbonate Reservoir and Its Model of Three-Element Controlling Reservoir: A Case Study from the Puguang Oilfield in Sichuan. *Acta Geologica Sinica*. **2010**, 84, (8), 1087-1094.
16. Zou, C.N.; Du, J.H.; Xu, C.C.; Wang, Z.C.; Zhang, B.M.; Wei, G.Q.; Wang, T.S.; Yao, G.; Deng, S.W.; Liu, J.J.; Zhou, H.; Xu, A.N.; Yang, Z.; Jiang, H.; Gu, Z.D., Formation, Distribution, Resource Potential and Discovery of the Sinian-Cambrian Giant Gas Field, Sichuan Basin, SW China. *Petrol Explor Dev+*. **2014**, 41, (3), 278-293.
17. Zhao, W.Z.; Wang, Z.C.; Jiang, H.; Fu, X.D.; Xie, W.R.; Xu, A.N.; Shen, A.J.; Shi, S.Y.; Huang, S.P.; Jiang, Q.C., Exploration Status of the Deep Sinian Strata in the Sichuan Basin: Formation Conditions of Old Giant Carbonate Oil/Gas Fields. *Natural Gas Industry B*. **2020**, 7, (5), 462-472.
18. Yang, Y.; Xie, J.R.; Zhao, L.Z.; Huang, P.H.; Zhang, X.H.; Chen, C.; Zhang, B.J.; Wen, L.; Wang, H.; Gao, Z.L.; Shan, S.J.,

Breakthrough of Natural Gas Exploration in the Beach Facies Porous Dolomite Reservoir of Middle Permian Maokou Formation in the Sichuan Basin and Its Implications: A Case Study of the Tridimensional Exploration of Well JT1 in the Central-Northern Sichuan Basin. *Natural Gas Industry B.* **2021**, 8, (4), 393-401.

19. Zhao, S.J.; Li, S.Z.; Suo, Y.H.; Guo, L.L.; Dai, L.M.; Jiang, S.H.; Wang, G., Structure and Formation Mechanism of the Yellow Sea Basin. *Earth Science Frontiers*. **2017**, 24, (4), 239-248.
20. Lei, B.H.; Xu, M.; Chen, J.W.; Liang, J.; Zhang, Y.G., Structural Characteristics and Evolution of the South Yellow Sea Basin since Indosinian. *China Geology*. **2018**, 1, (4), 466-476.
21. Xu, M.; Chen, J.; Liang, J.; Zhang, Y.; Lei, B.; Shi, J.; Wang, J.; Liu, J.; Liu, H., Basement Structures Underneath the Northern South Yellow Sea basin (East China): Implications for the Collision between the North China and South China Blocks. *J Asian Earth Sci*. **2019**, 186, 104040.
22. Chen, J.W.; Xu, M.; Lei, B.H.; Shi, J.; Liu, J., Collision of North China Yangtze Plates: Evidence from the South Yellow Sea. *Marine Geology and Quaternary Geology*. **2020**, 40, (3), 1-12.
23. Zhang, Y.G.; Chen, J.W.; Liang, J.; Ou, G.X.; Wu, D., Evidence of the Existence of Paleo Reservoirs in Laoshan Uplift of the South Yellow Sea Basin. *China Geology*. **2018**, 1, (4), 566-567.
24. Cai, L.X.; Xiao, G.L.; Guo, X.W.; Wang, J.; Wu, Z.Q.; Li, B.G., Assessment of Mesozoic and Upper Paleozoic Source Rocks in the South Yellow Sea Basin Based on the Continuous Borehole CSDP-2. *Mar Petrol Geol*. **2019**, 101, 30-42.
25. Cai, L.X.; Xiao, G.L.; Zeng, Z.G.; Zhang, X.H.; Guo, X.W.; Wang, S.P., New insights into Marine Hydrocarbon Geological Conditions in the South Yellow Sea Basin: Evidence from Borehole CSDP-2. *Journal of Oceanology and Limnology*. **2020**, 38, (4), 1169-1187.
26. Shinn, Y.J.; Chough, S.K.; Hwang, I.G., Structural Development and Tectonic Evolution of Gunsan Basin (Cretaceous–Tertiary) in the Central Yellow Sea. *Mar Petrol Geol*. **2010**, 27, (2), 500-514.
27. Tong, J.; Zhang, X.; Zhang, W.; Xiong, S., Marine Strata Morphology of the South Yellow Sea based on High-Resolution Aeromagnetic and Airborne Gravity Data. *Mar Petrol Geol*. **2018**, 96, 429-440.
28. Pang, Y.M.; Guo, X.W.; Chang, X.C.; Zhang, J.J.; Zhou, J.Q.; Cai, L.X., Characteristics and Classification of Paleozoic Tight Reservoirs in the Central Uplift of the South Yellow Sea Basin. *Energy Geoscience*. **2021**.
29. Bosence, D., Carbonate Reservoirs Porosity Evolution and Diagenesis in a Sequence Stratigraphic Framework. *Marine and Petroleum Geology - Mar Petrol Geol*. **2002**, 19, (10), 1295-1296.
30. Behrooz, E.D.; Hossain, R.B., Effects of Depositional and Diagenetic Characteristics on Carbonate Reservoir Quality: A Case Study from the South Pars Gas Field in the Persian Gulf. *Petrol Geosci*. **2009**, 15, (4), 325-344.
31. Wennberg, O.; Casini, G.; Jonoud, S.; Peacock, D., The Characteristics of Open Fractures in Carbonate Reservoirs and Their Impact on Fluid Flow: A Discussion. *Petrol Geosci*. **2016**, 22, (1), 91-104.
32. Wu, S.Y.; Chen, J.W.; Liang, J.; Liu, J.; Zhang, Y.G.; Yuan, Y., Characteristics of Mesozoic-Paleozoic Marine Carbonate Reservoir in the South Yellow Sea Basin and Hydrocarbon Accumulation: Comparison between the Sichuan Basin and the Subei basin. *Marine Geology Frontiers*. **2016**, 32, (1), 13-21.
33. Wu, S.Y.; Liu, J.; Chen, J.W.; Yuan, Y.; Liang, J.; Zhang, Y.G.; Shi, J., Pre-stack Simultaneous Inversion in the Marine Carbonate Reservoir Prediction of the South Yellow Sea Basin，China. *Acta Geologica Sinica (English Edition)*. **2019**, 93, (supp.2), 420-421.
34. Wu, S.Y.; Liu, J.; Chen, J.W.; LIANG, J.; Zhang, Y.G.; Yuan, Y.; Xu, M., Prediciton of pore-dominated Carboniferous-Lower Permian carbonate reservoir at the Laoshan Uplift, South Yellow Sea Basin. *Marine Geology and Quaternary Geology*. **2020**, 40, (5), 136-148.
35. Li, W.Y.; Liu, Y.X.; Xu, J.C., Onshore- Offshore Structure and Hydrocarbon Potential of the South Yellow Sea. *J Asian Earth Sci*. **2014**, 90, 127-136.

36. Shinn, Y.J., Geological Structures and Controls on Half- Graben Inversion in the Western Gunsan Basin, Yellow Sea. *Mar Petrol Geol*. **2015**, 68, 480-491.
37. Liang, J.; Zhang, P.H.; Chen, J.W.; Gong, J.M.; Yuan, Y., Hydrocarbon Preservation Conditions in Mesozoic-Paleozoic Marine Strata in the South Yellow Sea Basin. *Natural Gas Industry*. **2017**, (4), 432-441.
38. Duan, S.M.; Li, Y.G.; Pei, J.X.; Zhao, T.H.; Wu, Z.Q.; Han, B.; Yu, X.S.; Liu, L.J.; Chen, J.L.; Xu, Z.H., Carbonate Imaging with Magnetotellurics in a Shallow-Water Environment, South Yellow Sea, China. *J Appl Geophys*. **2020**, 178, 104076.
39. Yao, Y.J.; Chen, C.F.; Feng, Z.Q.; Ying, Z.S.; Hao, T.Y.; Wan, R.S., Tectonic Evolution and Hydrocarbon Potential in Northern Area of the South Yellow Sea. *J Earth Sci-China*. **2010**, 21, (1), 71 - 82.
40. Liu, J.; Zhang, X.H.; Mei, X.; Zhao, Q.H.; Guo, X.W.; Zhao, W.N.; Liu, J.X., The Sedimentary Succession of the Last ~3.50 Myr in the Western South Yellow Sea: Paleoenvironmental and Tectonic Implications. *Mar Geol*. **2018**, 47-65.
41. Pang, Y.M.; Guo, X.W.; Han, Z.Z.; Han, C.; Zhang, X.H.; Zhu, X.Q.; Hou, F.H.; Song, Z.G.; Xiao, G.L., Mesozoic – Cenozoic Denudation and Thermal History in the Central Uplift of the South Yellow Sea basin and the Implications for Hydrocarbon Systems: Constraints from the CSDP-2 Borehole. *Mar Petrol Geol*. **2019**, 99, 355-369.
42. Zhu, W.L.; Wu, J.F.; Zhang, G.C.; Ren, J.Y.; Zhao, Z.G.; Wu, K.Q.; Zhong, K.; Liu, S.X., Discrepancy Tectonic Evolution and Petroleum Exploration in China Offshore Cenozoic Basins. *Earth Science Frontiers*. **2015**, 22, (1), 88-101.
43. Zhang, Y.Q.; Xu, X.B.; Jia, D.; Shu, L.S., Deformation Record of the Change from Indosinian Collision-Related Tectonic System to Yanshanian Subduction-Related Tectonic System in South China during the Early Mesozoic. *Earth Science Frontiers (China University of Geosciences, Beijing; Peking University)*. **2009**, 16, (1), 234-247.
44. Xu, X.H.; Zhou, X.J.; Peng, J.N., Exploration Targets in Southern Yellow Sea through Analysis of Tectono-Depositional Evolution and Hydrocarbon Accumulation of Marine Basin in Yangtze Area. *Petroleum Geology & Experiment*. **2014**, 36, (5), 523-531+545.
45. Sun, J.; Wang, J.Q.; Gong, J.M., Abundance of Organic Matters in Mesozoic- Paleozoic Marine Source Rocks of Inland Area of the Lower Yangtze and Its Bearing on Lithofacies Paleogeography. *Marine Geology Frontiers*. **2016**, 32, (1), 22-28.
46. Gong, J.M.; Chen, J.W.; SUN, J.; Wang, J.Q.; Zhang, Y.G.; Liao, J.; Tian, R.C.; Cheng, Q.S.; Chen, Z.Q., Distribution of Source Rocks of the Gaojiabian Formation in the Lower Yangtze Areas and Its Implications for the South Yellow Sea Basin. *Marine Geology Frontiers*. **2016**, 32, (1), 43-47.
47. Zhu, W.L.; Chen, C.F.; Zhang, B.C.; Wan, Y.Z.; Fu, X.W.; Zhang, Y.G., Paleozoic Basin Prototype Evolution and Source Rock Development in the South Yellow Sea. *Petroleum Geology & Experiment*. **2020**, 42, (5), 728-741.
48. Liang, J.; Zhang, Y.G.; Dong, G.; Xiong, B.H., A Discussion on Marine Mesozoic- Paleozoic Reservoirs in South Yellow Sea. *Marine Geology & Quaternary Geology*. **2011**, 31, (5), 101-108.
49. Zhang, Y.G.; Chen, J.W.; Wu, S.Y.; Yuan, C.F.; Zhao, Y.H., Reservoir Prediction for Deposits from Hezhou Formation of Lower Carboniferous to Qixia Formation of Lower Permian on the Laoshan Uplift of the South Yellow Sea. *Marine Geology Frontiers*. **2016**, 32, (10), 60-64.
50. Chen, J.W.; Xu, M.; Lei, B.H.; Liang, J.; Zhang, Y.G.; Wu, S.Y.; Shi, J.; Yuan, Y.; Wang, J.Q.; Zhang, Y.X.; Li, G.; Wang, W.J., Prospective Prediction and Exploration Situation of Marine Mesozoic-Paleozoic Oil and Gas in the South Yellow Sea. *China Geology*. **2019**, 2, (1), 67-84.
51. Liang, J.; Chen, J.W.; Wang, J.Q.; Zhang, P.H.; Wu, S.Y.; Zhang, Y.G.; Yuan, Y.; Xu, M., Hydrocarbon Geological Conditions and Exploration Prospects of Marine Strata in the Laoshan Uplift, South Yellow Sea Basin. *Acta Geologica Sinica*. **2019**.
52. Xu, J.C.; Wu, C.P.; Wang, X.; Wu, Y., Characteristics of Source- Reservoir -Cap Rock and Hydrocarbon Prospect Evaluation in the South Yellow Sea. *Geological Survey of China*. **2017**, 4, (5), 60-65.
53. Chen, J.W.; Liang, J.; Zhang, Y.G.; Yang, C.Q.; Yuan, Y.; Xu, M.; Wang, J.Q.; Lei, B.H.; Li, G.; Yang, Y.Q.; Yang, C.S.;

Sun, J., Regional Evaluation of Oil& Gas Resources in Offshore China and Exploration of Oil and Gas in the Yellow Sea and East China Sea. *Marine Geology & Quaternary Geology*. **2019**, 39, (6), 1-29.

54. Guo, X.W.; ZHANG, X.H.; Wu, Z.Q.; XIAO, G.L.; Hou, F.H.; Liu, J., Scientific Objective and Preliminary Progresses of CSDP-2 Well in Continental Shelf Drilling Program. *Journal of Jilin University (Earth Science Edition)*. **2019**, 49, (1), 1-12.
55. Feng, Z.Q.; Yao, Y.; Zeng, X.H.; Wang, Q.; Wang, L.L.; Chen, Q.; Yi, H.; Jin, H.F., New Understanding of Mesozoic-Paleozoic Tectonics and Hydrocarbon Potential in Yellow Sea. *China Offshore Oil and Gas (Geology)*. **2002**, 16, (6), 367-373.
56. Hu, F., Hydrocarbon Resources Potential Study in Mesozoic-Paleozoic Marine Strata in the South Yellow Sea Bain. *Offshore Oil*. **2010**, 30, (3), 1-8+77.
57. Chen, J.W.; Zhang, Y.G.; Ou, G.X.; Liang, J.; Yuan, Y.; Wu, S., The Inclusion Evidence of Multi-Phase Hydrocarbon Accumulation in the South Yellow Sea. *Marine Geology Frontiers*. **2018**, 34, (2), 69-70.
58. Sheng, Q.Y.; Zheng, Q.F.; Wu, X.H.; Zhang, Y.Q.; Wang, X.D., Biostratigraphic and Sedimentological progress of the Carboniferous Hezhou Formation at Chaohu, Anhui province. *Journal of Stratigraphy*. **2013**, 37, (1), 41-47.
59. Ali, A.; Alves, T.M.; Saad, F.A.; Ullah, M.; Toqeer, M.; Hussain, M., Resource Potential of Gas Reservoirs in South Pakistan and Adjacent Indian Subcontinent Revealed by Post-Stack Inversion Techniques. *J Nat Gas Sci Eng*. **2018**, 49, 41-55.
60. Mahaman Salifou, I.A.; Zhang, H.; Boukari, I.O.; Harouna, M.; Cai, Z., New Vuggy Porosity Models-Based Interpretation Methodology for Reliable Pore System Characterization, Ordovician Carbonate Reservoirs in Tahe Oilfield, North Tarim Basin. *J Petrol Sci Eng*. **2021**, 196, 107700.
61. Liu, Y.J.; Lai, F.Q.; Zhang, H.J.; Tan, Z.J.; Wang, Y.F.; Zhao, X.T.; Tan, X.F., A Novel Mineral Composition Inversion Method of Deep Shale Gas Reservoir in Western Chongqing. *J Petrol Sci Eng*. **2021**, 202, 108528.
62. Clayton, R.N.; Epstein, S., Relationship between 18O/16O Ratios in Coexisting Minerals of Igneous and Metamorphic Rocks. *J Geol*. **1958**, 66, (4), 345-371.
63. Keith, M.L.; Weber, J.N., Carbon and Oxygen Isotopic Composition of Selected Limestones and Fossils. *Geochim Cosmochim Ac*. **1964**, 28, (11), 1787-1816.
64. Pekar, S.F.; McHugh, C.M.G.; Christie-Blick, N.; Jones, M.; Carbotte, S.M.; Bell, R.E.; Lynch-Stieglitz, J., Estuarine Processes and Their Stratigraphic Record: Paleosalinity and Sedimentation Changes in the Hudson Estuary (North America). *Mar Geol*. **2004**, 209, (1-4), 113-129.
65. Sampei, Y.; Matsumoto, E.; Dettman, D.L.; Tokuoka, T.; Abe, O., Paleosalinity in a Brackish Lake during the Holocene based on Stable Oxygen and Carbon Isotopes of Shell Carbonate in Nakaumi Lagoon, Southwest Japan. *Palaeogeography, Palaeoclimatology, Palaeoecology*. **2005**, 224, (4), 352-366.
66. Lécuyer, C.; Daux, V.; Moissette, P.; Cornée, J.; Quillévéré, F.; Koskeridou, E.; Fourel, F.; Martineau, F.; Reynard, B., Stable Carbon and Oxygen Isotope Compositions of Invertebrate Carbonate Shells and the Reconstruction of Paleotemperatures and Paleosalinities- A Case Study of the Early Pleistocene of Rhodes, Greece. *Palaeogeography, Palaeoclimatology, Palaeoecology*. **2012**, 350-352, 39-48.
67. Craig, H., Isotopic Standards for Carbon and Oxygen and Correction Factors for Mass- Spectrometric Analysis of Carbon Dioxide. *Geochim Cosmochim Ac*. **1957**, 12, 133-149.
68. Shi, G.R.; Chen, Z.Q., Lower Permian Oncolites from South China; Implications for Equatorial Sea-Level Responses to Late Palaeozoic Gondwanan Glaciation. *J Asian Earth Sci*. **2006**, 26, (3-4), 424-436.
69. Armstrong-Altrin, J.S.; Lee, Y.I.; Verma, S.P.; Worden, R.H., Carbon, Oxygen, and Strontium Isotope Geochemistry of Carbonate Rocks of the Upper Miocene Kudankulam Formation, Southern India: Implications for Paleoenvironment and Diagenesis. *Geochemistry*. **2009**, 69, (1), 45-60.
70. Hong, H.L.; Zhao, H.; Zhang, L.F.; Jia, Z.H.; Li, Q.Z.; Zhou, T.F., The Early Carboniferous Zircon U-Pb chronology and Its

Sedimentary Significance in the Northern Chaohu area, Anhui, East China. *Acta Petrol Sin*. **2014**, 30, (4), 1087-1096.

71. Li, S.Y.; Jiang, D.; Zhao, Y.Y.; Hu, X.M.; Shi, Y.K., Carboniferous- Early Permian Carbonate Microfacies and Sedimentay Environments in the Chaohu Region, Anhui. *Sedimentary Geology and Tethyan Geology*. **2015**, 35, (1), 3-15.
72. Ross, C.A.; Ross, J.R.P.; Ross, C.A.; Haman, D., Late Paleozoic Sea Levels and Depositional Sequences. *Special Publications - Cushman Foundation for Foraminiferal Research*. **1987**, 24, 137-149.
73. Ross, C.A.; Ross, J.R.P., Late Paleozoic Depositional Sequences Are Synchronous and Worldwide. *Geology*. **1995**, 13, 194-197.
74. Wang, C.S.; Li, X.H.; Chen, H.D.; Tan, J.X., Permian Sea- Level Changes and Rising- Falling Events in South China. *ACTA Sedimentologica Sinica*. **1999**, 17, (4), 39-44.
75. Mcelhinny, M.W., Permian Paleomagnetism of the Western Yangtze Block, China: A Reinterpretation. *J Geodyn*. **1985**, 2, (2), 115-117.
76. Wu, Y.W.; Tian, H.; Li, T.F.; Ji, S.; Liu, Z.Y.; Xiao, X.M.; Xie, L.H., Enhanced Terrestrial Organic Matter Burial in the Marine Shales of Yangtze Platform during the Early Carboniferous Interglacial Interval. *Mar Petrol Geol*. **2021**, 129, 105064.
77. Zhao, M.Y.; Zheng, Y.F., Marine carbonate records of terrigenous input into Paleotethyan seawater: Geochemical constraints from Carboniferous limestones. *Geochim Cosmochim Ac*. **2014**, 141, 508-531.
78. Feng, Z.Z.; He, Y.B.; Wu, S.H., Lithofacies paleography of Permian in Middle and Lower Yangtze region. *ACTA sedimentaologica Sinica*. **1993**, 11, (3), 13-24.
79. Li, S.Y.; Jin, F.Q., Carboniferous Paleography in the Lower Yangtze Basin. *Journal of Hefei University of Technology*. **1994**, 17, (3), 167-174.
80. Li, R.F.; Liu, B.P.; Zhao, C.L., Correlation of Carboniferous Depositional Sequences on the Yangtze Plate with Others on a Global Scale. *ACTA Sedimentology Sinica*. **1997**, 15, (3), 25-30.
81. Qie, W.K.; Zhang, X.H.; Du, Y.S.; Zhang, Y., Lower Carboniferous Carbon Isotope Stratigraphy in South China: Implications for the Late Paleozoic Glaciation. *Science China Earth Sciences*. **2011**, 54, (1), 84-92.
82. Wu, S.Q.; Yan, J.X.; Liu, K.; Yan, Y.J., Response of Early Permian Siliciclastic Depositional System to the Advance of Gondwana Glaciation in Southwestern Guizhou. *Earth Science Frontiers*. **2016**, 23, (6), 299-311.
83. Heckel, P.H., Sea-Level Curve for Pennsylvanian Eustatic Marine Transgressive-Regressive Depositional Cycles along Midcontinent Outcrop Belt, North America. *Geology*. **1986**, 14, 330-334.
84. Smith Jr., L.B.; Read, J.F., Rapid onset of Late Paleozoic Glaciation on Gondwana: Evidence from Upper Mississippian Strata of the Midcontinent, United States. *Geology*. **2000**, 28, 279-282.
85. Feldman, H.R.; Franseen, E.K.; Joeckel, R.M.; Heckel, P.H., Impact of Longer-Term Modest Climate Shifts on Architecture of High-Frequency Sequences (Cyclothems), Pennsylvanian of Midcontinent U.S.A. *J Sediment Res*. **2005**, 75, (3), 350-368.
86. Veevers, J.J.; Powell, C.M., Late Paleozoic Glacial Episodes in Gondwanaland Reflected in Transgressive-Regressive Depositional Sequences in Euramerica. *Geol Soc Am Bull*. **1987**, 98, 475-487.
87. Chen, J.W.; Gong, J.M.; Li, G.; Li, H.J.; Yuan, Y.; Zhang, Y.X., Great Resources Potential of the Marine Mesozoic- Paleozoic in the South Yellow Sea Basin. *Marine Geology Frontiers*. **2016**, 32, (1), 1-7.
88. Gao, X.H.; Zhang, X.H.; Guo, X.W.; Cai, L.X.; Hou, F.H.; Zhu, X.Q., Provenance and Tectonic Implications of Paleozoic Strata in the South Yellow Sea Basin, China – Revealed from the Borehole CSDP-2. *J Ocean U China*. **2020**, 19, (3), 536-550.
89. Wang, R.X.; Wang, Q.F.; Huang, Y.X.; Yang, S.J.; Liu, X.F.; Zhou, Q., Combined Tectonic and Paleogeographic Controls on the Genesis of Bauxite in the Early Carboniferous to Permian Central Yangtze Island. *Ore Geol Rev*. **2018**, 101, 468-480.
90. Chen, H.C.; Wang, Y.H.; Yan, Y.Y., Early Carboniferous Strata in the South of Jiangsu and Anhui. *ACTA Stratigraphic Sinica*. **1979**, 3, (4), 242-250.

91. Zhao, M.Y.; Zheng, Y.F., Marine Carbonate Records of Terrigenous Input into Paleotethyan Seawater: Geochemical Constraints from Carboniferous Limestones. *Geochim Cosmochim Ac*. **2014**, 141, 508-531.
92. Al-Ramadan, K.A.; Hussain, M.; Imam, B.; Saner, S., Lithologic Characteristics and Diagenesis of the Devonian Jauf Sandstone at Ghawar Field, Eastern Saudi Arabia. *Mar Petrol Geol*. **2004**, 21, (10), 1221-1234.
93. Madden, R.H.C.; Wilson, M.E.J., Diagenesis of a SE Asian Cenozoic Carbonate Platform Margin and Its Adjacent Basinal Deposits. *Sediment Geol*. **2013**, 286-287, 20-38.
94. Abdullah, A.M.; Guillaume, D.; Philippe, R.; Yves-Michel, L.N., Carbon and Oxygen Isotope Stratigraphy of Jurassic Platform Carbonates from Saudi Arabia: Implications for Diagenesis, Correlations and Global Paleoenvironmental Changes. *Palaeogeography, Palaeoclimatology, Palaeoecology*. **2018**, 511, 388-402.
95. Fu, M.Y.; Song, R.C.; Gluyas, J.; Zhang, S.N.; Huang, Q., Diagenesis and Reservoir Quality of Carbonates Rocks and Mixed Siliciclastic as Response of the Late Carboniferous Glacio-Eustatic Fluctuation: A Case Study of Xiaohaizi Formation in Western Tarim Basin. *J Petrol Sci Eng*. **2019**, 177, 1024-1041.
96. Fu, Q.L.; Hu, S.Y.; Xu, Z.H.; Zhao, W.Z.; Shi, S.Y.; Zeng, H.L., Depositional and Diagenetic Controls on Deeply Buried Cambrian Carbonate Reservoirs: Longwangmiao Formation in the Moxi – Gaoshiti Area, Sichuan Basin, Southwestern China. *Mar Petrol Geol*. **2020**, 117, 104318.
97. Wang, W.G.; Lin, C.Y.; Zhang, X.G.; Dong, C.M.; Ren, L.H.; Lin, J.L., Discussion of Seismic Diagenetic Facies of Deep Reservoir in the East China Sea Basin. *J Petrol Sci Eng*. **2022**, 208, 109352.
98. Li, W.; Zhang, Z.J.; Dang, L.R., Depositional Systems and Evolution of the Upper Carboniferous Huanglong Formation in the Eastern Sichuan Basin. *Petrol Explor Dev+*. **2011**, 38, (4), 400-409.
99. Lin, C.M.; Huang, Z.C.; Liu, J.R.; Ling, H.F.; Zhang, S.; Zhao, Y.Y., Carboniferous Microfacies and Sequence Stratigraphy of Fenghuangshan Profile in Chaohu of Anhui province, China. *Acta Petrol Sin*. **2002**, 18, (3), 424-433.
100. Vai, G.B., Development of the Palaeogeography of Pangaea from Late Carboniferous to Early Permian. *Palaeogeography, Palaeoclimatology, Palaeoecology*. **2003**, 196, 125-155.
101. Li, N.; Wang, C.; Zong, P.; Mao, Y., Coevolution of Global Brachiopod Palaeobiogeography and Tectonopalaeogeography during the Carboniferous. *Journal of Palaeogeography*. **2021**, 10, (1).
102. Tabor, N.J.; Poulsen, C.J., Palaeoclimate Across the Late Pennsylvanian – Early Permian tropical palaeolatitudes: A Review of Climate Indicators, Their Distribution, and Relation to Palaeophysiographic Climate Factors. *Palaeogeography, Palaeoclimatology, Palaeoecology*. **2008**, 268, (3-4), 293-310.
103. Wang, Y.; Jin, Y.G., Permian Palaeogeographic Evolution of the Jiangnan Basin, South China. *Palaeogeography, Palaeoclimatology, Palaeoecology*. **2000**, 160, (1-2), 35-44.
104. Cai, L.X.; Zhang, X.H.; Guo, X.W.; Zeng, Z.G.; Xiao, G.L.; Pang, Y.M.; Wang, S.P., Effective Hydrocarbon-Bearing Geological Conditions of the Permian Strata in the South Yellow Sea Basin, China: Evidence from Borehole CSDP-2. *J Petrol Sci Eng*. **2021**, (196), 1-21.